# EFFECT OF BOUNDARY CONDITIONS ON PERFORMANCE OF POROELASTOGRAPHIC IMAGING TECHNIQUES IN NON HOMOGENEOUS POROELASTIC MEDIA

A Thesis

by

ANUJ CHAUDHRY

Submitted to the Office of Graduate Studies of
Texas A&M University
in partial fulfillment of the requirements for the degree of

MASTER OF SCIENCE

December 2010

Major Subject: Electrical Engineering

Effect of Boundary Conditions on Performance of

Poroelastographic Imaging Techniques in

Non Homogenous Poroelastic Media

# EFFECT OF BOUNDARY CONDITIONS ON PERFORMANCE OF POROELASTOGRAPHIC IMAGING TECHNIQUES IN NON-HOMOGENEOUS POROELASTIC MEDIA

A Thesis

by

ANUJ CHAUDHRY

Submitted to the Office of Graduate Studies of
Texas A&M University
in partial fulfillment of the requirements for the degree of

MASTER OF SCIENCE

Approved by:

| | |
|---|---|
| Chair of Committee, | Raffaella Righetti |
| Committee Members, | J.N. Reddy |
| | Jim Ji |
| | Shankar Bhattacharyya |
| Head of Department, | Costas Georghiades |

December 2010

Major Subject: Electrical Engineering

ABSTRACT

Effect of Boundary Conditions on Performance of Poroelastographic Imaging Techniques in Non Homogenous Poroelastic Media. (December 2010)

Anuj Chaudhry, B.E, Mumbai University, India

Chair of Advisory Committee: Dr. Raffaella Righetti

In the study of the mechanical behavior of biological tissues, many complex tissues are often modeled as poroelastic systems due to their high fluid content and mobility. Fluid content and fluid transport mechanisms in tissues are known to be highly correlated with several pathologies. Thus, imaging techniques capable of providing accurate information about these mechanisms can potentially be of great diagnostic value.

Ultrasound elastography is an imaging modality that is currently used as a complement to sonographic methods to detect a variety of tissue pathologies. Poroelastography is a new elastographic technique that has been recently proposed to image the mechanical behavior of tissues that can be modeled as poroelastic media. The few poroelastographic studies retrievable focus primarily on homogeneous poroelastic media. In this study, a statistical analysis of the performance of poroelastographic techniques in a non-homogeneous poroelastic simulation model under different loading conditions was carried out. The two loading conditions simulated were stress relaxation (application of constant strain) and creep compression (application of constant stress), both of which have been commonly used in the field of poroelastography. Simulations

were performed using a FE poroelastic simulation software combined with ultrasound simulation software techniques and poroelastography processing algorithms developed in our laboratory. The non-homogeneous poroelastic medium was modeled as a cube (background) containing a cylindrical inclusion (target). Different permeability, Young's modulus and Poisson's ratio contrasts between the underlying matrix of the background and the target were considered. Both stress relaxation and creep compression loading conditions were simulated. The performance of poroelastography techniques was quantified in terms of accuracy, elastographic contrast–to–noise ratio and contrast transfer efficiency.

The results of this study show that, in general, image quality of both axial strain and effective Poisson's ratio poroelastograms is a complex function of time, which depends on the contrast between the poroelastic material properties of the background and the poroelastic material properties of the target and the boundary conditions. The results of this study could have important implications in defining the clinical range of applications of poroelastographic techniques and in the methodologies currently deployed.

# ACKNOWLEDGEMENTS

I would like to thank my committee chair, Dr Raffaella Righetti for her constant support, patience, motivation and constructive criticism. Without her selfless help, guidance and belief in me this work would not have been possible. She has and will always be my greatest source of inspiration. I am grateful to Dr. Ginu for not only providing us with the FEM data but also for being very helpful in patiently answering all my queries about them. I would also like to thank Dr. Reddy for his constant support and guidance.

Finally, thanks to my family, friends and my lab mates Sanjay, Biren and Xu who have been a support system throughout my stay with the Ultrasound Imaging group.

# NOMENCLATURE

| | |
|---|---|
| SR | Stress Relaxation |
| AS | Axial Strain |
| PR | Poisson’s Ratio |
| TC | Time Constant |
| EPR | Effective Poisson’s Ratio |
| CNRe | Axial Strain Elastogram Contrast to Noise Ratio |
| PCNRe | Effective Poisson’s Ratio Elastogram Contrast to Noise Ratio |
| CTE | Contrast Transfer Efficiency |

# TABLE OF CONTENTS

CHAPTER Page

# LIST OF FIGURES

FIGURE Page

FIGURE Page

FIGURE Page

# LIST OF TABLES

# CHAPTER I

# INTRODUCTION

## 1. Introduction

In the study of the mechanical behavior of biological tissues, many complex tissues are often modeled as poroelastic systems due to their high fluid content and mobility (Armstrong and Mow 1982, Mridha and Odman 1986). Fluid content and fluid transport mechanisms in tissues are known to be highly correlated with several pathologies. For example, cancerous tissues possess altered fluid transport properties with respect to normal tissues (Folkman 1992).Lymphedema, a disease commonly following cancer therapies, manifests as an abnormal accumulation of fluids with impaired mobility (Mridha and Odman. 1986).

Ultrasound elastography is an imaging modality that is currently used as a complement to sonographic methods to detect a variety of tissue pathologies primarily related to cancers. Poroelastography is a new elastographic technique that has been recently proposed to image the mechanical behavior of poroelastic tissues (Konofagou et al. 2001, Righetti et al. 2004, Righetti et al. 2005, and Righetti et al 2007a). In poroelastographic methods, tissues are often modeled as biphasic media. Their mechanical behavior under uniaxial compression is characterized by a number of tissue parameters, which include the elastic properties of the solid matrix, the permeability,

---

This thesis follows the style of Ultrasound in Medicine and Biology.

the viscous drag between solid and fluid phases and the boundary conditions (Armstrong et al. 1984).

The few poroelastographic studies retrievable in the literature focus on imaging the behavior of homogeneous poroelastic media. No attempt has been made yet at investigating the performance of poroelastography techniques in non-homogeneous media, presumably due to the challenges related to modeling such media. In this thesis, we present a simulation study that investigates in a systematic manner the performance of poroelastographic techniques using a non-homogeneous tissue model. The simulation model used in this study is chosen as a possible representation of tumors in soft tissues.

In addition, in the field of poroelastography two loading techniques are commonly used: stress relaxation (application of constant strain) and creep (application of constant stress) compressions. The loading conditions may in general affect the resulting strain distributions and, consequently, the quality of the resulting poroelastographic images. Currently, there is no systematic study, which compares the performance of poroelastography techniques when using these two loading methods. The need for such a study has been suggested in previous literature (Righetti et al. 2007b, Nair 2010).

This work represents the first attempt at analyzing the performance of poroelastography for imaging non-homogeneous poroelastic media under different boundary conditions. Therefore, the results of this study could have important implications in defining the clinical range of applications of poroelastographic

echniques and in the methodologies currently deployed in poroelastography experiments.

## 2. Objective and hypothesis

The objective of this thesis is to statistically analyze the performance of poroelastography when imaging non homogeneous poroelastic media under different boundary conditions. The fundamental hypothesis driving this study is that the image quality of poroelastographic techniques in non homogeneous poroelastic media is dependent on both the underlying mechanical contrast provided by the poroelastic tissue parameters (namely, permeability, Young's modulus and Poisson's ratio) and the boundary conditions. Further, it is hypothesized that poroelastographic image quality factors are time-dependent due to the temporal nature of the mechanical behavior of poroelastic materials caused by the underlying fluid transport mechanisms.

## 3. Research plan

*Design and implement a simulation tool to describe the poroelastic behavior of non-homogeneous media*

The Image formation model consists of a mechanical Finite Element Model (FEM) to simulate poroelastic materials, an ultrasound simulation model and an elastography module. The mechanical poroelastic model provides the temporal displacement data at each node in the poroelastic simulated media under compression. These displacement data are the input to a software program that generates simulated

temporal ultrasonic RF frames. The simulated frames are then used to generate simulated elastograms using elastographic algorithms developed in our laboratory. The simulated elastograms include: axial strain elastograms, effective Poisson's ratio elastograms and poroelastograms.

*Define a FEM model suitable to test the hypothesis of the study*

Define geometry, mechanical parameters of interest and boundary conditions to be tested. The model used in this study consists of a cube (simulating a soft tissue background) containing a cylindrical inclusion (simulating a tumor) having different poroelastic properties. The different internal boundary conditions are simulated by varying the contrast between the poroelastic parameters of the background and poroelastic parameters of the inclusion . These include: Young's modulus and Poisson's ratio of the solid matrix and permeability of the solid matrix to the pore fluid. The external boundary conditions analyzed in this study are: stress relaxation and the creep compression.

*Assess image quality of resulting poroelastographic images*

Analyze the performance of simulated poroelastographic images in terms of the following image quality parameters: elastographic contrast-to-noise ratio (CNRe), elastographic contrast, accuracy and contrast transfer efficiency (CTE).

*Statistically analyze image quality results*

Standard statistical tests (student t-test) are performed to analyze the resulting poroelastographic image quality factors and discern significant differences among the various simulated testing conditions.

## 4. Motivations of the presented work

*Imaging of tumors*

This work represents the first systematic study that focus on poroelastographic models that can approximate soft tissue lesions. Many cancerous tissues posses different fluid flow properties than the surrounding tissues (Netti et al. 1995). Interstitial hypertension, i.e. elevated interstitial fluid pressures (IFP), is a well-known characteristic of soft tissues tumors (Less et al. 1992; Netti et al. 1995) and is known to be closely related to the tissue's permeability (Milosevic et al. 2008; Khosravani et al. 2004). The findings of this work may aid in designing *in vivo* experiments to image and characterize these tumors.

*Monitoring treatment of tumors*

Several cancer treatments are known to modify the permeability of tumors (Park et al. 2002). Thus, poroelastography could provide a valuable diagnostic tool to monitor changes in fluid patterns as a consequence to tissue treatments.

*Design of experimental poroelastography methods*

The work presented in this study can serve to design new and efficient poroelastographic experimental set-ups to optimize image quality parameters in tissues.

**5. Structure of thesis**

Chapter II discusses some basic concepts on poroelasticity pertinent to the presented study and reviews previous work done in the field of poroelastography. Chapter III provides a description of the simulation, image quality and statistical methods used in this study. Chapter IV shows and discusses the results of this work. Chapter V presents the conclusions and opportunities for future work in this area.

# CHAPTER II

# BASIC CONCEPTS ON POROELASTICITY AND POROELASTOGRAPHY

## 1. Introduction

This chapter reviews some of the concepts at the basis of poroelasticity theories relevant for this study and presents a brief summary of previous work pertinent to the field of poroelastography.

## 2. Poroelasticity

Biot's work from 1935 to 1941 (Biot 1935, Biot et al. 1941) is often considered the basics for the theory of linear poroelasticity, although earliest work on poroelasticity was developed for soil mechanics by Terzaghi (1923). More recently, Bowen (1982) and Mow et al. (1980) proposed the use of mixture theory. These theories have developed from the consolidation theory and have been widely used to model the poroelastic behavior of tissues. According to these theories, a poroelastic medium can be defined as a multiphasic space in which at least one of the phases is not solid (Detournay and Cheng 1993). For many tissues the number of phases can be limited to two, i.e., a solid phase, which defines the interstitial matrix, and a fluid phase, which defines the interstitial fluid (Armstrong et al. 1984). For one-dimensional geometry, a poroelastic material may be completely characterized by three parameters (Armstrong et al 1984): the Young's modulus of the solid matrix; the Poisson's ratio of the solid matrix and the permeability of the poroelastic medium.

The Effective Poisson's ratio (EPR) of a poroelastic tissue is related to the effective compressibility of the material, which depends on the ease with which it can allow fluid movement and change volume under compression (Wang 2000). The permeability ($\kappa$) of a poroelastic medium is given by Darcy (1856) as

$$q = -\frac{\kappa}{\mu}\nabla p \tag{2.1}$$

where $q$ is the fluid volume flowing through a region of unit cross sectional area per unit time, $\mu$ is the viscosity of the fluid and $\nabla p$ is the pressure gradient across the region.Two excellent reviews of biphasic theories may be found in Rice and Cleary (1976) and Wang (2000). Here, we will briefly recall some major concepts, which are relevant in the context of the work presented in this paper. The time-dependent mechanical behavior of a poroelastic tissue under sustained compression is governed by the interaction between the solid matrix phase and the pore fluid phase. During sustained loading, solid matrix deformation and fluid translocation occur in the tissue due to established pressure gradients (Wang 2000). The magnitude of this phenomenon is determined by the viscous drag between the solid and the fluid phases and depends on the effective compressibility properties of the material (both of the solid matrix and of the pore fluid), elastic and permeability properties of the solid matrix as well as the boundary conditions (Mow et al. 1980, Armstrong et al. 1984).

The two limiting cases of "fast" and "slow" loading are referred to "undrained" and "drained" conditions, respectively. . The undrained condition occurs when the pores are fully saturated by the fluid and no fluid is allowed in or out of the material. The drained condition occurs when the fluid is forced to flow in or out of the material such

that the pore pressure remains constant. Hence for a poroelastic medium under uniaxial loading three temporal stages can be observed: 1) Instantaneously after loading, the material behaves like an incompressible solid. The stress is fully supported by the fluid phase, which increases the pore pressure; 2) The stress is then partially transferred to the solid matrix, and fluid begins to exude. During this transient time, the pore pressure decays as the solid matrix consolidates; 3) When the equilibrium condition is reached ( drained condition), fluid flow ceases and the pore pressure drops to zero.

Biological tissues are usually modeled as incompressible elastic solids with some exceptions such as brain, cartilage, and cornea that are known to be partially compressible (Fatt 1968). Poroelastic tissues, however, are by definition compressible. Pathologies can also alter the compressibility properties of a tissue (Mridha and Ödman 1986). Tumors of the breast, for example, behave like partially compressible solids (Poisson's ratio < 0.5) even though their individual phases may be incompressible (Netti et al. 1995; Van Houten et al 2003). These tissues are expected to exhibit the spatial and temporal patterns characteristic of poroelastic tissues. Estimating and imaging such patterns could greatly aid in the assessment of many pathological conditions.

## 3. Background on poroelastography

Ultrasound elastography is a well established imaging modality used to map the local strains of a soft tissue under quasi-static compression (Ophir et al. 1991; Ophir et al. 1999). The technique has been used as a complementary modality to sonography to image tumors in soft tissues in vivo (Qiu et al. 2008). Poroelastography is a novel

elastographic technique that aims at imaging the temporal mechanical behavior of poroelastic tissues. The motivation behind the development of poroelastography comes from the observation that a tissue's temporal response is affected by pathology. Thus, quantification of this response may help in the diagnosis and treatment of many diseases, including cancers (Mridha and Odman. 1986, Righetti et al. 2007b, Qiu et al. 2008).

Konofagou et al. (2001) reported the first simulation work on poroelastography, which showed the feasibility of mapping local EPR in uniform homogeneous poroelastic media. The time-sequenced elastograms obtained by dividing corresponding pairs of lateral strain and axial strain elastograms were defined as "poroelastograms" . The exact nomenclature used to describe poroelastographic images can be found in Appendix A of this thesis. A few years later, Fortin et al. (2003) showed experimental curves depicting the temporal decay of the mean EPR in cartilage discs. Righetti et al. (2004) reported the first experimental poroelastographic images. This work demonstrated, for the first time, the practical feasibility of experimentally imaging temporal and spatial EPR distributions in uniform poroelastic phantoms. A few years later, the same group proposed a method to quantify the temporal changes in the axial strain and EPR poroelastograms using curve fitting methods (Righetti et al. 2005, Righetti et al. 2007b). These studies included an attempt to apply poroelastography to non homogeneous poroelastic media, suggesting the feasibility but with no assessment on the image quality. Berry et al. (2006a, 2006b) proposed a curve fitting method to compute various poroelastic parameters from the EPR curves obtained from uniform poroelastic media. Liederman and Barbone (2006) used a tumor mechanical model

described by Netti et al. (1995) to map temporal changes in axial strain distribution. Once again, this simulation study showed the technical feasibility to elastographic image poroelastic lesions but did not tackle image quality issues of fundamental importance to fully predict the potentials of this methodology when applied to real tissues. Currently, there is no formal study that focus on the assessment of the performance of poroelastography on non-homogeneous materials and quantifies the effects of internal and external boundary conditions, which are known to play a major role on the temporal behavior of poroelastic tissues (Righetti et al. 2007a; Righetti et al. 2005) .

# CHAPTER III

# METHODS

## 1. Introduction

This chapter describes the simulation, image quality and statistical methods used in this study. The methodology consists of a simulation tool, which is used to generate the simulated poroelastograms, followed by a statistical analysis of the image quality of the generated poroelastographic images.

## 2. Simulation framework

The simulation framework is formed by three fundamental parts (see also Figure 1). The first part represents the mechanical poroelastic module. The mechanical poroelastic module provides with temporal displacement data at specified nodes in the simulated poroelastic medium under sustained compression. The ultrasonic RF data generation module uses the displacements resulting from the mechanical poroelastic module and provides as output the simulated temporal ultrasound RF data. Finally, the elastography module processes the simulated RF data to generate the axial strain and EPR poroelastograms. Figure 1 shows a schematic of the simulation framework. Individual modules are explained in the sections below.

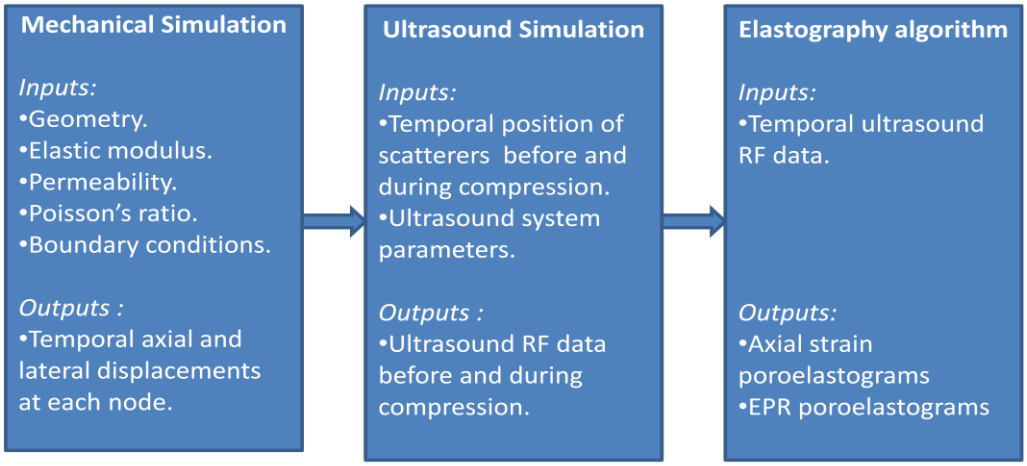


Fig 1. Schematic of the image formation model.

*Mechanical poroelastic module*

In general, in this module we need to formulate: geometry of the problem, material parameters, boundary conditions and meshing parameters. Once all these parameters are formulated, the FEM solution is provided by an in-house simulation software (courtesy of Dr. Reddy's group in the Mechanical Engineering Department at Texas A&M University). This software assumes a linear stress-strain behavior of the solid phase and a single fluid flowing through the saturated media obeying Darcy's flow law. These two phases are coupled using Biot's constant (alpha) and the specific storage coefficient, which depends on the undrained and drained material properties. Once the basic equations are set up, the finite element development with the displacement and pressure as the primary variables is carried out.

In this study, we simulated a 40 mm cubical poroelastic media with a 10 mm diameter cylindrical inclusion (see Fig. 2) .Various Young's modulus (E), permeability

(K) and Poisson's Ratio (Nu) contrasts between the target and the background were simulated. Table 1 shows the various combinations of material parameters analyzed in this study. The baseline material parameters used in this simulation study were chosen based on previous experimental work carried out by our group (Righetti et al. 2005). Each case is simulated for both stress relaxation and creep loading boundary conditions .The in-house simulation code, proprietary of Dr. Reddy's group, provides with the temporal and spatial positions of the nodes in the simulated media. The overall window of observation of the time-dependent poroelastic phenomena occurring in the simulated media was chosen as 600 s. This value was chosen based on previous experimental work carried out by our group (Righetti et al. 2005, Nair 2010). Due to the high computational time required for processing the simulated data, the period between successive frames was fixed at 10 s.

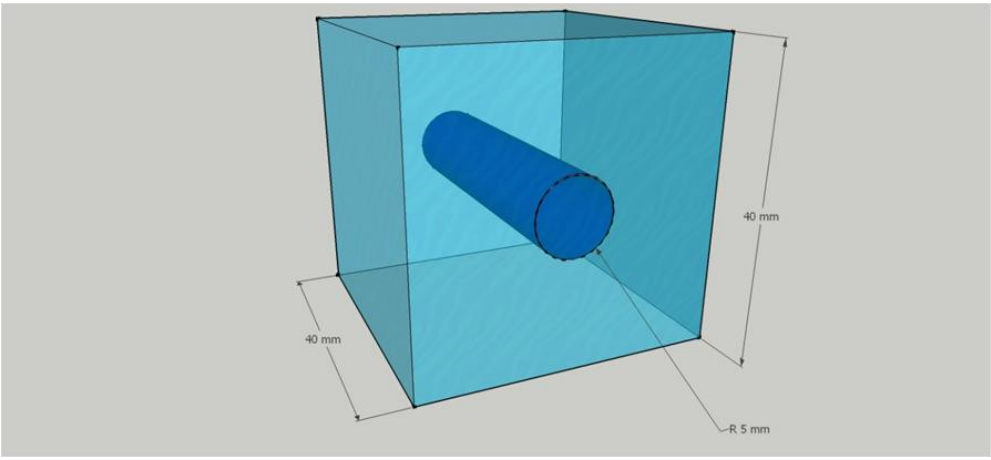


Fig 2. Geometry of the mechanical model.

Table 1. Material properties of the simulated media. (E is the Young's modulus, V is the drained Poisson's ratio and K is the permeability of the solid matrix to the interstitial fluid).

| **E=1.73*10$^{3}$ Pa** | **K=1.95*10$^{-10}$ m$^{4}$/N.s** | | | | **V=0.25** | | |
|---|---|---|---|---|---|---|---|
| | **BACKGROUND** | | | | **INCLUSION** | | |
| **Model 1 : No contrast** | **E** | **K** | **v** | | **E** | **K** | **v** |
| **Model 2 Permeability contrast** | **E** | **K** | **v** | | **E** | **10$^{-4}$*K** | **v** |
| | **E** | **K** | **v** | | **E** | **10$^{-2}$*K** | **v** |
| | **E** | **K** | **v** | | **E** | **10$^{+2}$*K** | **v** |
| | **E** | **K** | **v** | | **E** | **10$^{+4}$*K** | **v** |
| **Model 3 Elastic contrast** | **E** | **K** | **v** | | **10$^{-2}$*E** | **K** | **v** |
| | **E** | **K** | **v** | | **10$^{-1}$*E** | **K** | **v** |
| | **E** | **K** | **v** | | **10$^{+1}$*E** | **K** | **v** |
| | **E** | **K** | **v** | | **10$^{+2}$*E** | **K** | **v** |
| **Model 4 Poisson's ratio contrast** | **E** | **K** | **v** | | **E** | **K** | **1.8*V** |
| | **E** | **K** | **v** | | **E** | **K** | **0.2*V** |

*Ultrasound simulation module*

A Convolution Model was used to generate temporal ultrasound RF data, similar to the one proposed by Srinivasan et al. 2003. A schematic of the RF data generation simulation module is shown in Figure 3. In this simplistic model, the system's point spread function (PSF) was modeled as a Gaussian-modulated cosine pulse. The scattering function was modeled as a normal distribution . At each point in the simulated media, the RF signal was computed by convolving the scattering function and the point spread function. . In all models, a scatterer density of at least 40 scatterers/pulse-width was used, satisfying the requirement for obtaining fully developed Rayleigh backscatterers. The speed of sound was fixed at 1540 m/s. The sonographic signal-to-noise ratio ($SNR_s$) of the fundamental signals was set at 40 dB. We simulated an ultrasound system that resembled our experimental ultrasound system. The simulated ultrasound transducer had 128 elements, frequency bandwidth between 5-14 MHz, a 6.6 MHz center frequency and 50% fractional bandwidth at -6 dB. The transducer's beamwidth was assumed to be dependent on the wavelength and to be approximately 1 mm at 6.6 MHz. The sampling frequency was set at 40 MHz. The same process was used to generate temporal RF frames by using the corresponding mechanical displacements obtained from the FEM model. Bilinear interpolation was performed on the input mechanical displacement data prior the computation of the simulated RF frames. The in-house ultrasound simulation software was implemented in C. All simulations were run on an Intel® Core ™ 2 Duo CPU @ 2 GHz and 2 GB RAM.

*Elastography module*

The elastography module was used to generate the simulated poroelastographic images. Technical details regarding this algorithm can be found in Yang et al. (2009) . Below, I briefly summarize the steps required to generate an elastogram

To compute each pair of simulated temporal axial strain and EPR elastogram corresponding to a given time $t_x$ during compression, the simulated mechanical data corresponding to time $t = 0^-$ i.e., before loading, and the simulated mechanical data corresponding to the time $t = t_x$ i.e., during loading, were used. Axial and later displacements were first estimated using time delay estimation techniques. While there exit several time delay estimation techniques that can be used for elastography (Srinath 2010), the correlation-based methods are known to provide the optimal estimates (in the mean squared error sense). Thus, a cross-correlation algorithm developed in our laboratory was used. In this algorithm, echo lines corresponding to pre and post compression signals are divided into temporal windows of equal length, and their time delay is estimated by locating the peak of cross correlation function.

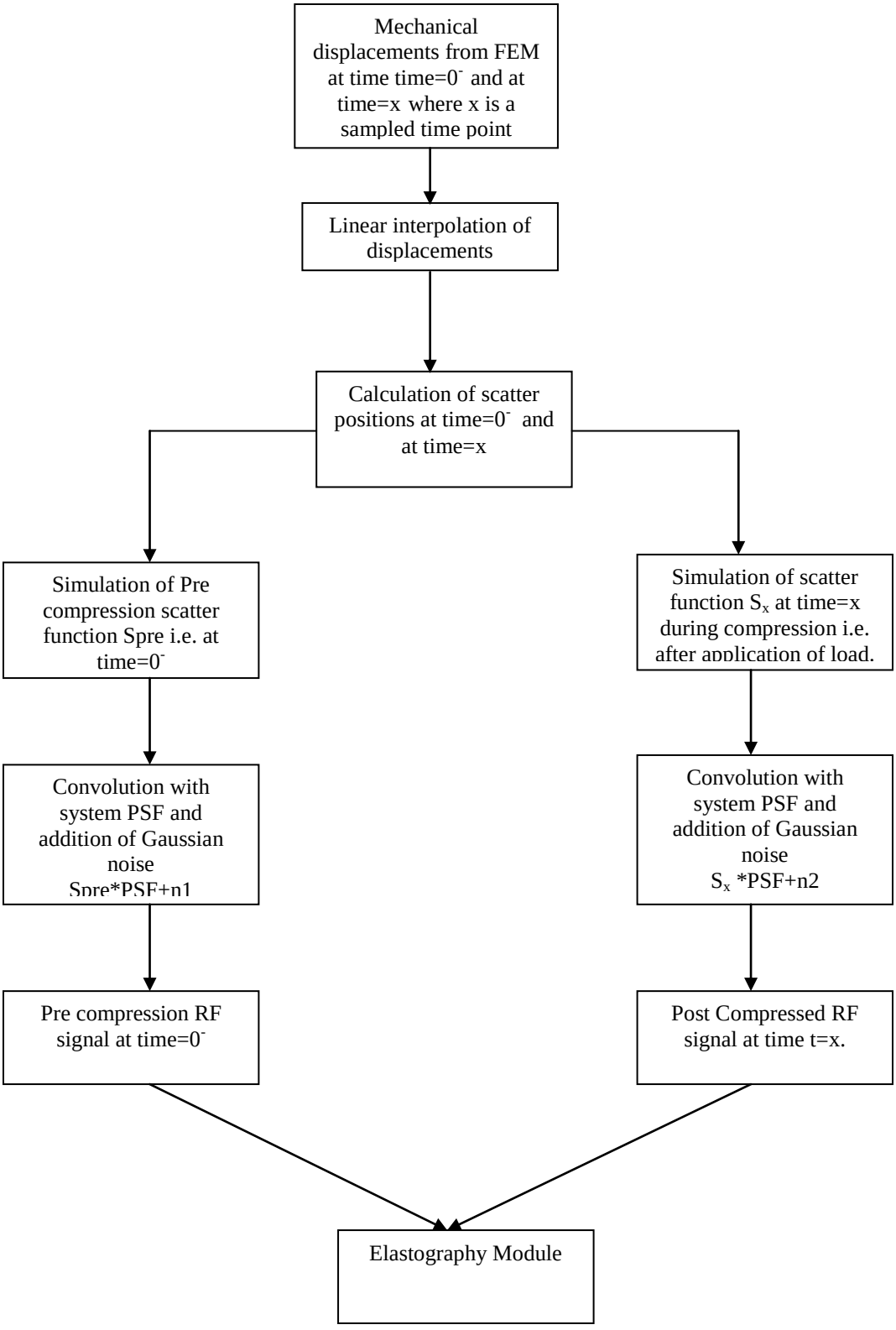


Fig 3. Schematic of RF data generation

Global and adaptive stretching methods are used to improve elastographic signal-to-noise ratio (Varghese and Ophir 1997). Once the axial and lateral displacements are obtained, the axial strain and lateral strain are computed using a staggered strain estimation method (Srinivasan et al. 2002). Effective Poisson's ratio elastograms are then generated by dividing the lateral strain elastogram by the matching pixels of the axial strain elastogram. To speed up computation, the algorithm is executed on massively parallel GPGPU (Yang et al. 2009).

In addition to the axial strain and EPR temporal elastograms, in selected cases, it is also possible to generate time constant (TC) elastograms (Nair. 2010). TC elastograms are generated by applying curve fitting techniques to each pixel in a poroelastogram (Righetti et al. 2005). In my study, 50 independent realizations of both axial strain and EPR ratio elastograms were considered for the statistical analysis (Bendat and Piersol 2000).

## 3. Image quality analysis

Image quality analysis was performed using the following elastographic image quality factors:

*Axial strain Contrast to Noise Ratio (CNRe)*

*CNRe* is a measure of detectability of a lesion . It is mathematically defined as (Srinivasan et al. 2003):

$$CNR_e = \frac{2(s_t - s_b)^2}{\sigma_t^2 + \sigma_b^2} \tag{3.1}$$

where St is the mean strain in the inclusion or the target, Sb is the mean strain in the background and σt and σb are the corresponding standard deviations.

*Poisson's ratio Contrast to Noise Ratio (PCNRe)*

Similarly as for the axial case, the Poisson's ratio contrast to noise ratio for an inclusion inside a homogeneous background is defined as (Righetti et.al 2007a)

$$PCNR_e = \frac{2(\nu_t - \nu_b)^2}{\sigma_{\nu_t}^2 + \sigma_{\nu_b}^2}, \tag{3.2}$$

where $\nu_t$ is the estimated Poisson's ratio of the inclusion and $\nu_b$ is the estimated Poisson's ratio of the background.

*Accuracy*

Accuracy by definition is the error between the estimated parameter and the true parameter. In our simulation study, the true mechanical displacements obtained from FEM were used to generate the ideal or true axial strain and EPR maps. The mean of the absolute difference between the axial strain elastograms and the ideal strain maps ($\mu_{dt}$) was used to calculate the accuracy using the following formula:

$$\text{Axial strain elastography accuracy} = \left(1 - \frac{\mu_{dt}}{\mu_i}\right) \times 100 \tag{3.3}$$

where $\mu_{dt}$ is the mean of the de-trended image and $\mu_i$ is the mean of the ideal image. Since I observed prominent spatial strain distribution patterns in the background of both ideal images and computed elastograms generated by fluid translocation effects, the poroelastographic images needed to be detrended prior computation of the aforementioned image quality factors.

*Contrast Transfer Efficiency (CTE)*

In 1995, Ponnekanti et al. investigated the dependence of axial strain elastographic contrast to the true underlying elastic modulus contrast. The difference between these two contrasts was defined as the "Contrast Transfer Efficiency" (CTE). The same worked, showed that the ratio between the mean strain in the inclusion and the mean strain in the background is not equal to the ratio between the elastic modulus of the inclusion and the elastic modulus of the background. This is a fundamental mechanical limitation of elastography that depends on the boundary conditions (Varghese et al. 2001, Kallel et al. 1996).

The CTE in poroelastography applications is currently unknown. Here, the estimation of the CTE is more problematic because is the axial strain and EPR elastograms are expected to be influenced several mechanical properties of the underlying matrix, including (at least) Young's modulus, Poisson's ratio and permeability .Hence to quantify the CTE in poroelastography, I isolated the effect of each of these parameters.

I defined the CTE of the axial strain and EPR with respect to the underlying Young's modulus contrast as in Ponnekanti et.al (1995) and as a function of time.

$$\eta = \frac{Co}{Ct} = \frac{\mu i/\mu b}{Ct} \tag{3.4}$$

where $Co$ is the observed image contrast, $\mu i$ is the calculated mean strain inside inclusion, $\mu b$ is the calculated mean strain on the background, $Ct$ is the true underlying contrast and $\eta$ is the CTE. The CTE of the axial strain and EPR with respect to the underlying permeability contrast were defined as the ratio between the TC of the EPR poroelastograms to the true underlying permeability contrast given as:

$$\eta = \frac{\tau i/\tau b}{Ct} \tag{3.5}$$

where $,\tau b$ are the TC of the mean EPR of the inclusion and the background respectively and $Ct$ is the true underlying permeability contrast. The explanation behind this definition is that temporal changes in poroelastograms are dependent on the rate at which fluid translocates within the poroelastic phantom. As the background and the inclusion have different permeability properties, fluid will flow at different rates which can be approximately estimated by calculating the time constants of the decay in EPR elastograms. When the only poroelastic contrast is provided by an underlying permeability contrast, this ratio should be a direct representation of the true permeability contrast.

The CTE of the axial strain and EPR with respect to the underlying Poisson's ratio contrast was defined as for the permeability CTE but evaluated with respect to the underlying true Poisson's ratio contrast and given as:

$$\eta = \frac{\tau i/\tau b}{Ct} \tag{3.6}$$

In this case $Ct$ is the true underlying Poisson's ratio contrast.

**4. Statistical analysis of the results**

Image quality parameters (CNRe and accuracy) were statistically compared for SR and creep loading conditions by using the student t-test. For p values greater than 0.05 the difference was concluded to be statistically significant.

# CHAPTER IV

# SIMULATION RESULTS

## 1. Introduction

In this chapter, I show the major results of this work. A brief discussion of each of the results is provided. I analyzed all cases given in Table 1 in the previous chapter. Following each result, a statistical analysis comparing stress relaxation and creep boundary conditions for the various quality factors analyzed in this study is presented.

## 2. Permeability contrast

Fig 4 to Fig 7 show ideal axial strain maps and corresponding axial strain poroelastograms obtained for a background/inclusion permeability contrast of -40 dB (Fig. 4), -20 dB (Fig. 5), +20 dB (Fig. 6), and + 40 dB ( Fig. 7) both for the stress relaxation (SR) and the creep compression loading conditions.

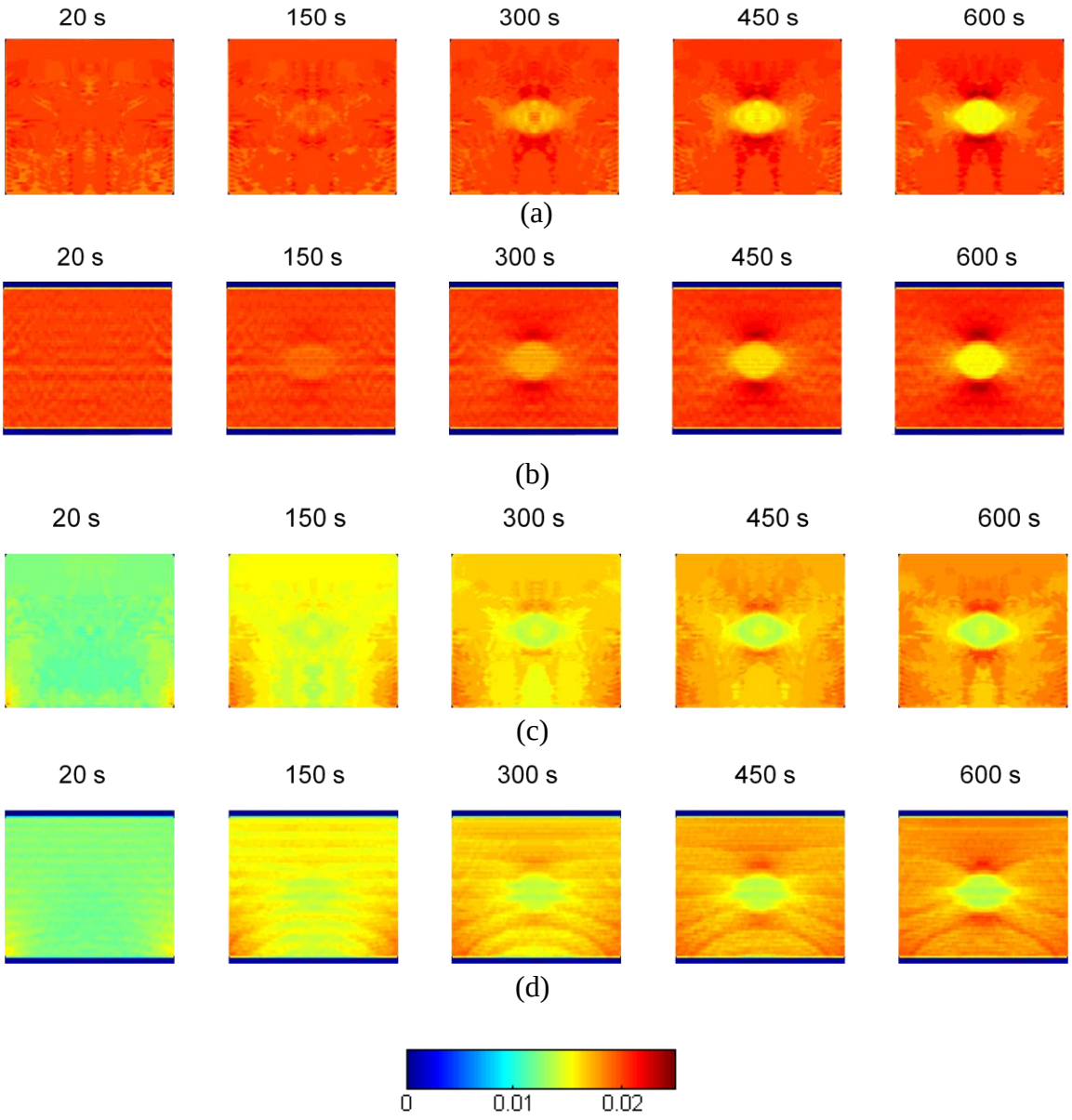


Figure 4 .Time-sequenced axial strain images for -40db permeability contrast between inclusion and background. (a) Ideal strain maps and (b) corresponding axial strain poroelastogram obtained under SR (c). Ideal strain maps and (d) corresponding axial strain poroelastogram obtained under creep compression. . In each case images are displayed for time values equal to 20s, 150s ,300s and 600s as indicated in the figure.

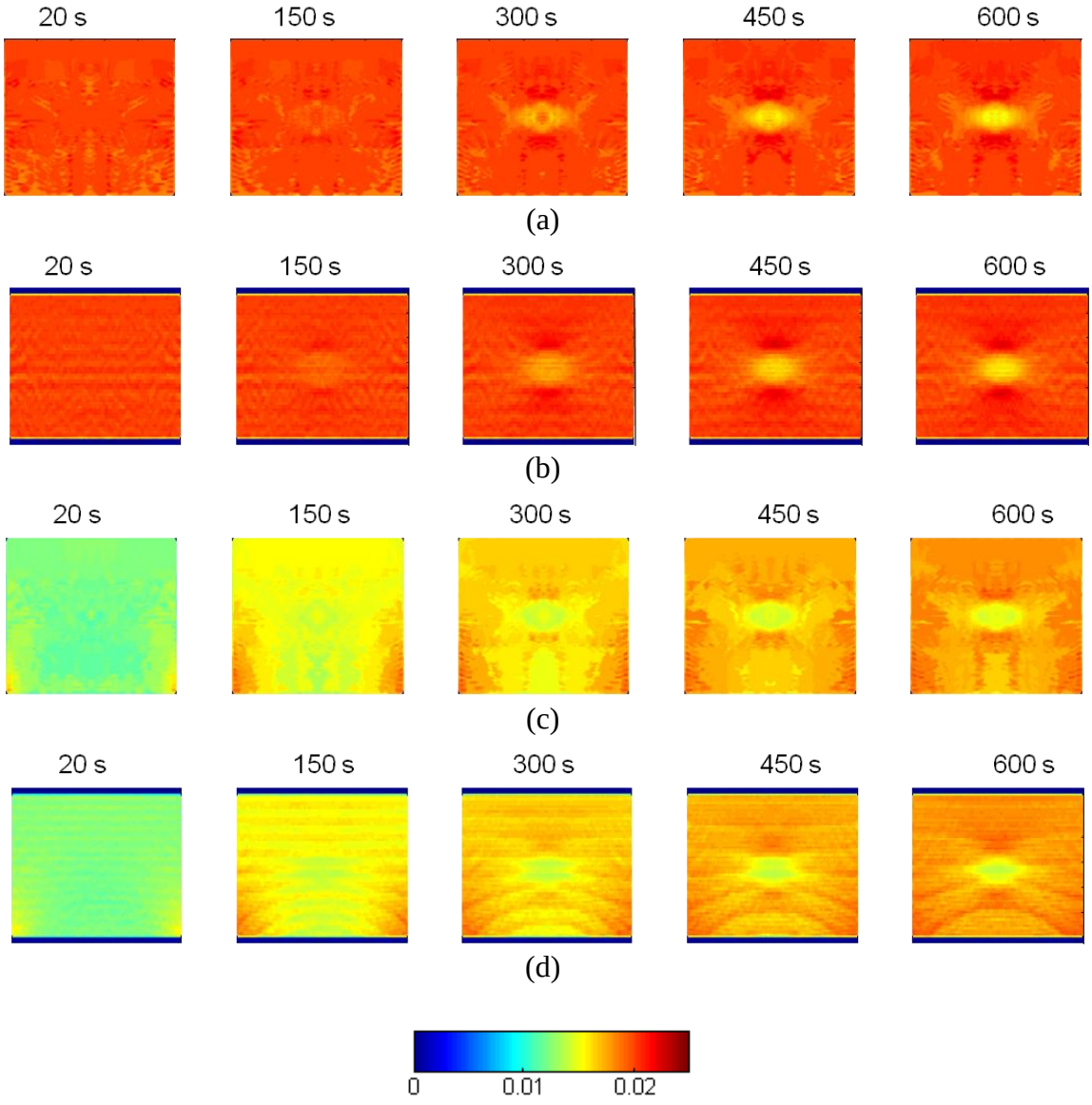


Figure 5. Time-sequenced axial strain images for -20db permeability contrast between inclusion and background. (a) Ideal strain maps and (b) corresponding axial strain poroelastogram obtained under SR (c). Ideal strain maps and (d) corresponding axial strain poroelastogram obtained under creep compression. In each case images are displayed for time values equal to 20s, 150s ,300s and 600s as indicated in the figure.

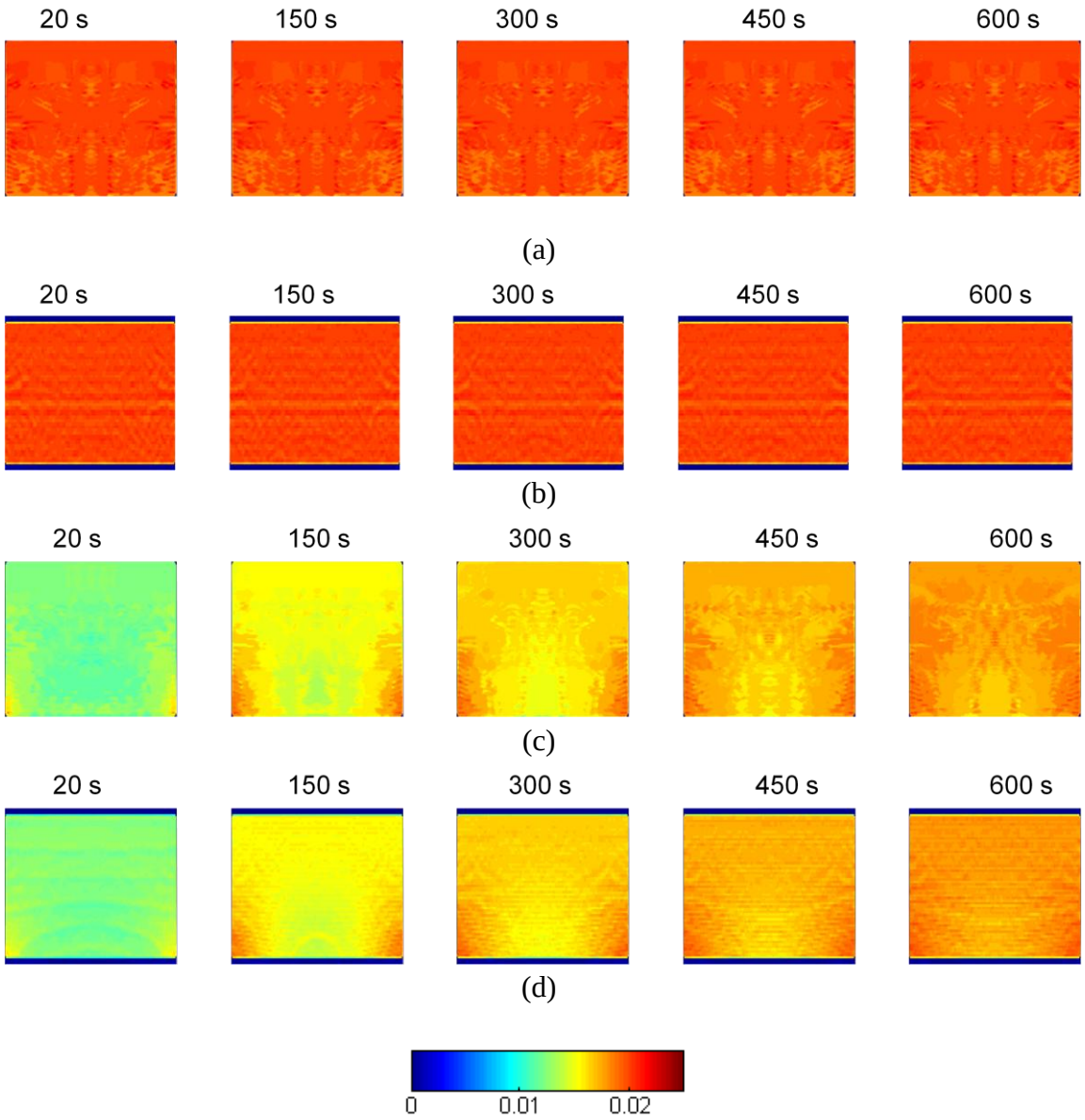


Figure 6.Time-sequenced axial strain images for +20db permeability contrast between inclusion and background. (a) Ideal strain maps and (b) corresponding axial strain poroelastogram obtained under SR (c). Ideal strain maps and (d) corresponding axial strain poroelastogram obtained under creep compression. In each case images are displayed for time values equal to 20s, 150s ,300s and 600s as indicated in the figure.

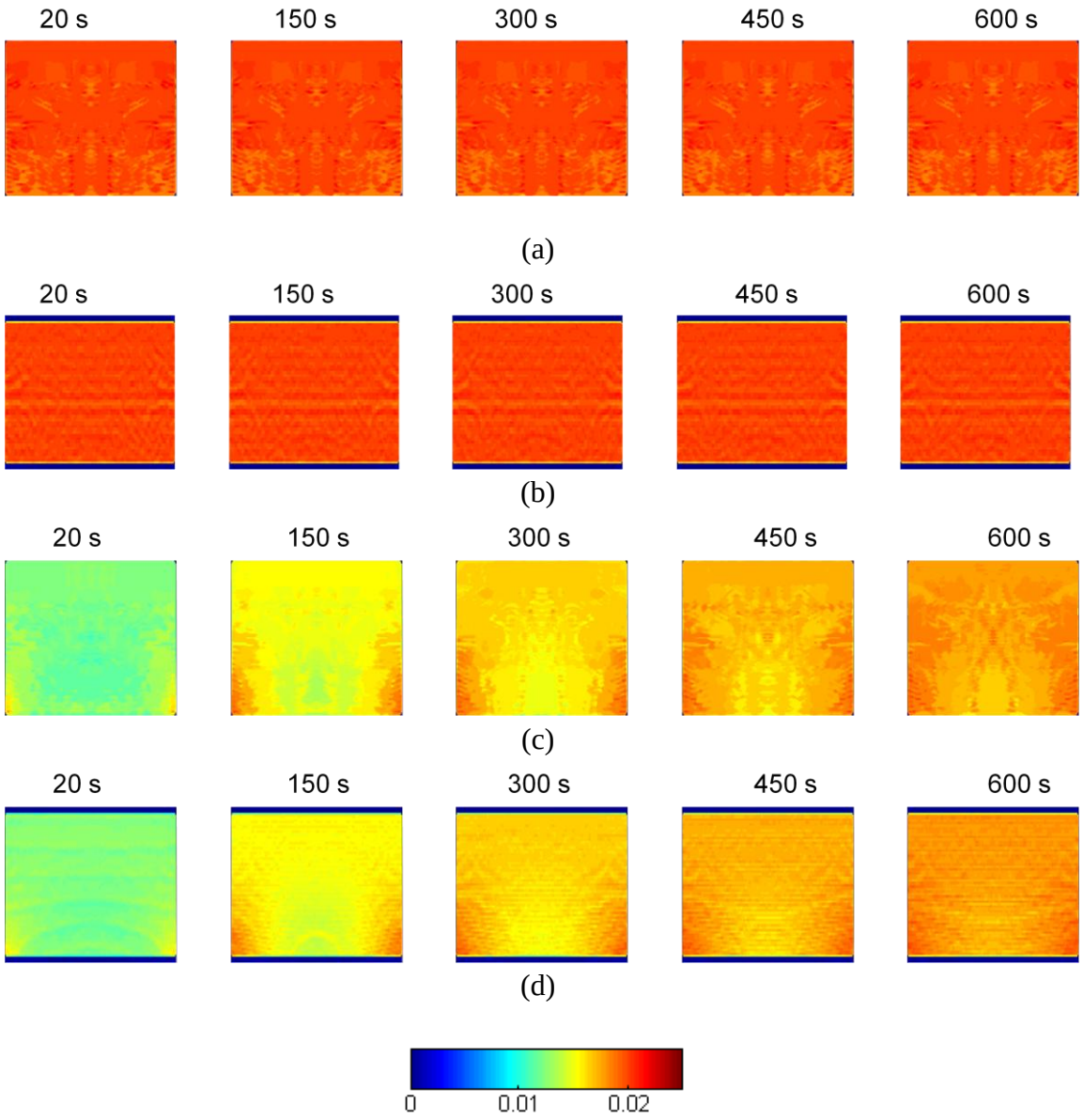


Figure 7.Time-sequenced axial strain images for +40db permeability contrast between inclusion and background. (a) Ideal strain maps and (b) corresponding axial strain poroelastogram obtained under SR (c). Ideal strain maps and (d) corresponding axial strain poroelastogram obtained under creep compression. In each case images are displayed for time values equal to 20s, 150s ,300s and 600s as indicated in the figure.

*Permeability contrast CNRe analysis*

Figure 8 shows a three dimensional plot of CNRe as a function of time and the true underlying permeability contrast. It can be observed that CNRe increases with increasing contrast when the background is more permeable than inclusion and is almost zero when the background is less permeable than the inclusion.

In addition, the plot suggests that the CNRe increases with time as the inclusion becomes more and more visible (see Figures 4-7) and there exists a crossover point somewhere between 300 s and 400 s between the CNRe corresponding to the SR loading condition and the CNRe corresponding to the creep condition.

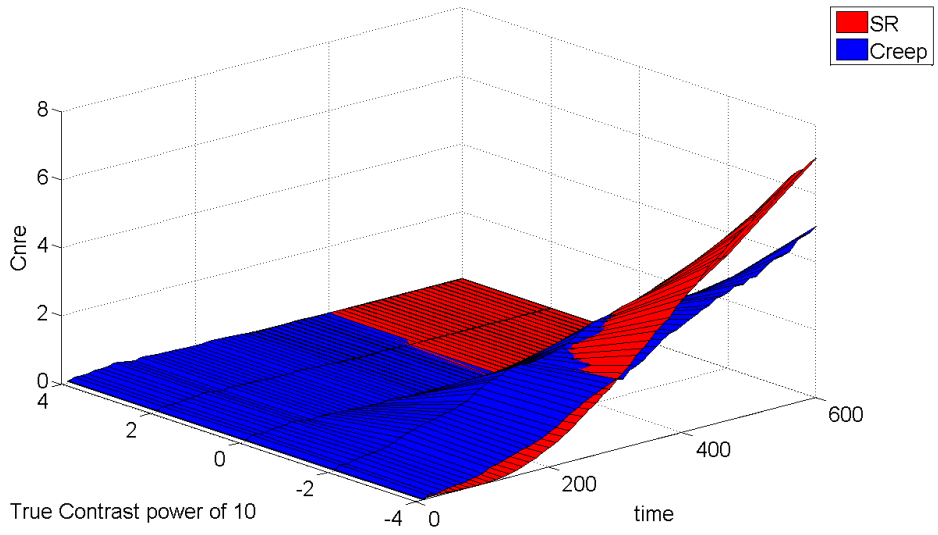


Fig 8 .CNRe plot for permeability contrast.

*Statistical analysis of comparison between SR and creep*

Since CNRe is a measure of contrast between inclusion and background, I performed the statistical analysis of significant difference only for cases where the inclusion can be seen in the corresponding axial strain poroelastograms.

*Case1: -40db contrast between inclusion and background*

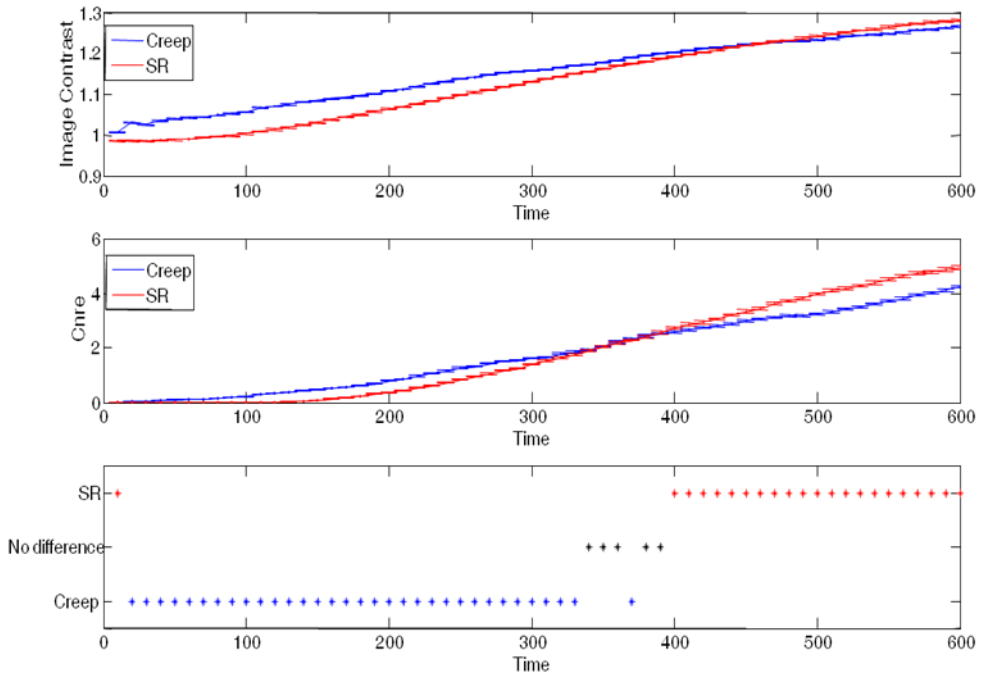


Figure 9. Statistical comparison of CNRe for -40db permeability contrast between inclusion and background .From top to bottom : Image contrast as a function of time for SR (red) and creep(blue) (error bars represent the 95% confidence interval), CNRe as a function of time for SR (red) and creep(blue) (error bars represent the 95% confidence interval) and summary of the t-testing comparing the results obtained using the two compression techniques .

*Case2: -20db contrast between inclusion and background*

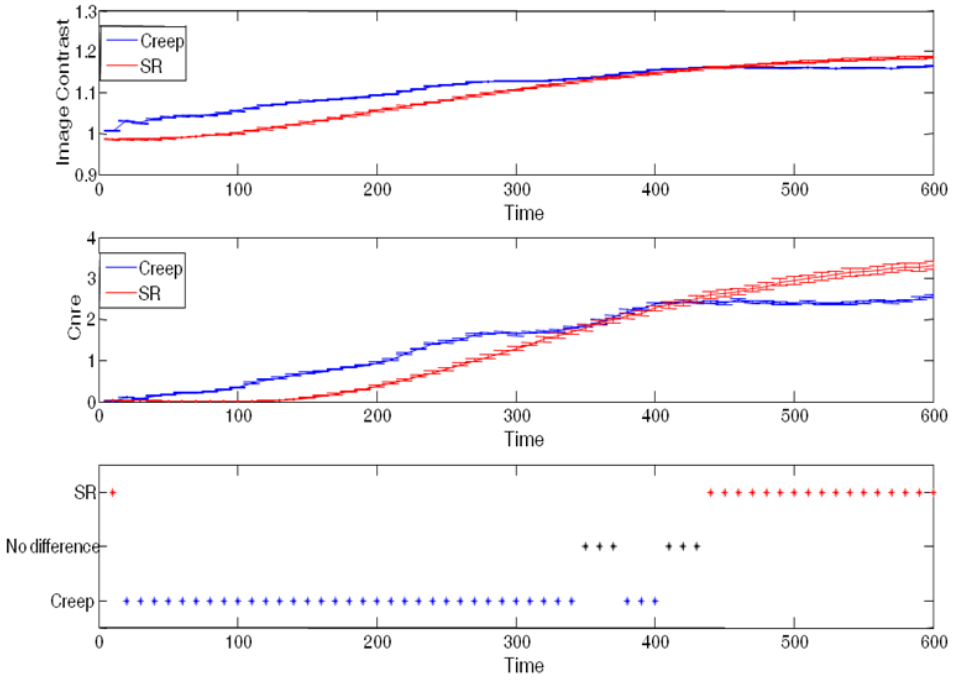


Figure 10. Statistical comparison of CNRe for -20db permeability contrast between inclusion and background .From top to bottom : Image contrast as a function of time for SR (red) and creep(blue) (error bars represent the 95% confidence interval), CNRe as a function of time for SR (red) and creep(blue) (error bars represent the 95% confidence interval) and summary of the t-testing comparing the results obtained using the two compression techniques .

From Figures 9 and 10, we can observe that initially, the creep compression method leads to statistically higher CNRe values. A crossover point is reached at around 350 s. After this point, the SR compression method leads to statistically higher CNRe values.

*Axial strain poroelastogram accuracy analysis for permeability contrast*

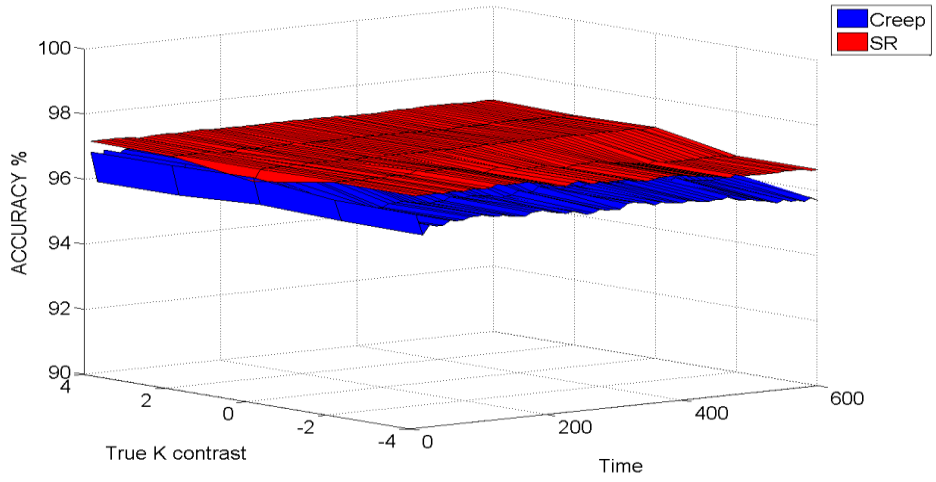


Fig 11. Accuracy of axial strain poroelastograms vs. time vs. underlying permeability contrast.

The accuracy plot generated in Figure 11 for axial strain poroelastograms shows that accuracy is very high (> 90%) for both the SR and creep cases. Another interesting observation is that accuracy stays fairly constant with respect to both time and underlying contrast Accuracy of SR is statistically better than that of creep.

*Effective Poisson's Ratio (EPR) poroelastography*

Figures 12 -15 show the EPR poroelastograms for permeability contrast along with the corresponding ideal EPR maps generated by using the mechanical displacements obtained from FEM simulations.

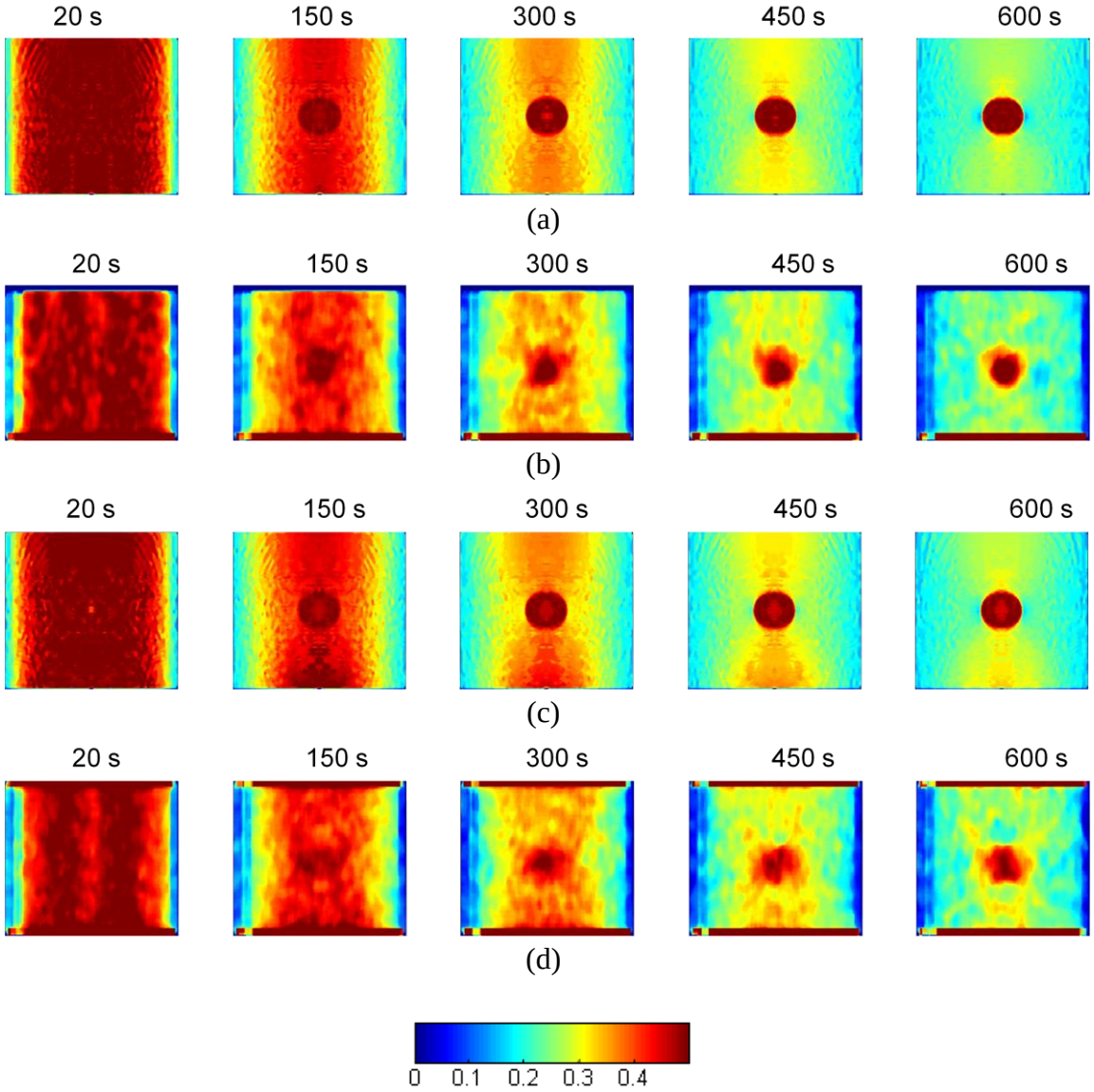


Figure 12. Time-sequenced EPR images for -40db permeability contrast between inclusion and background. (a) Ideal EPR maps and (b) corresponding EPR poroelastogram obtained under SR (c). Ideal EPR maps and (d) corresponding EPR poroelastogram obtained under creep compression. In each case images are displayed for time values equal to 20s, 150s ,300s and 600s respectively.

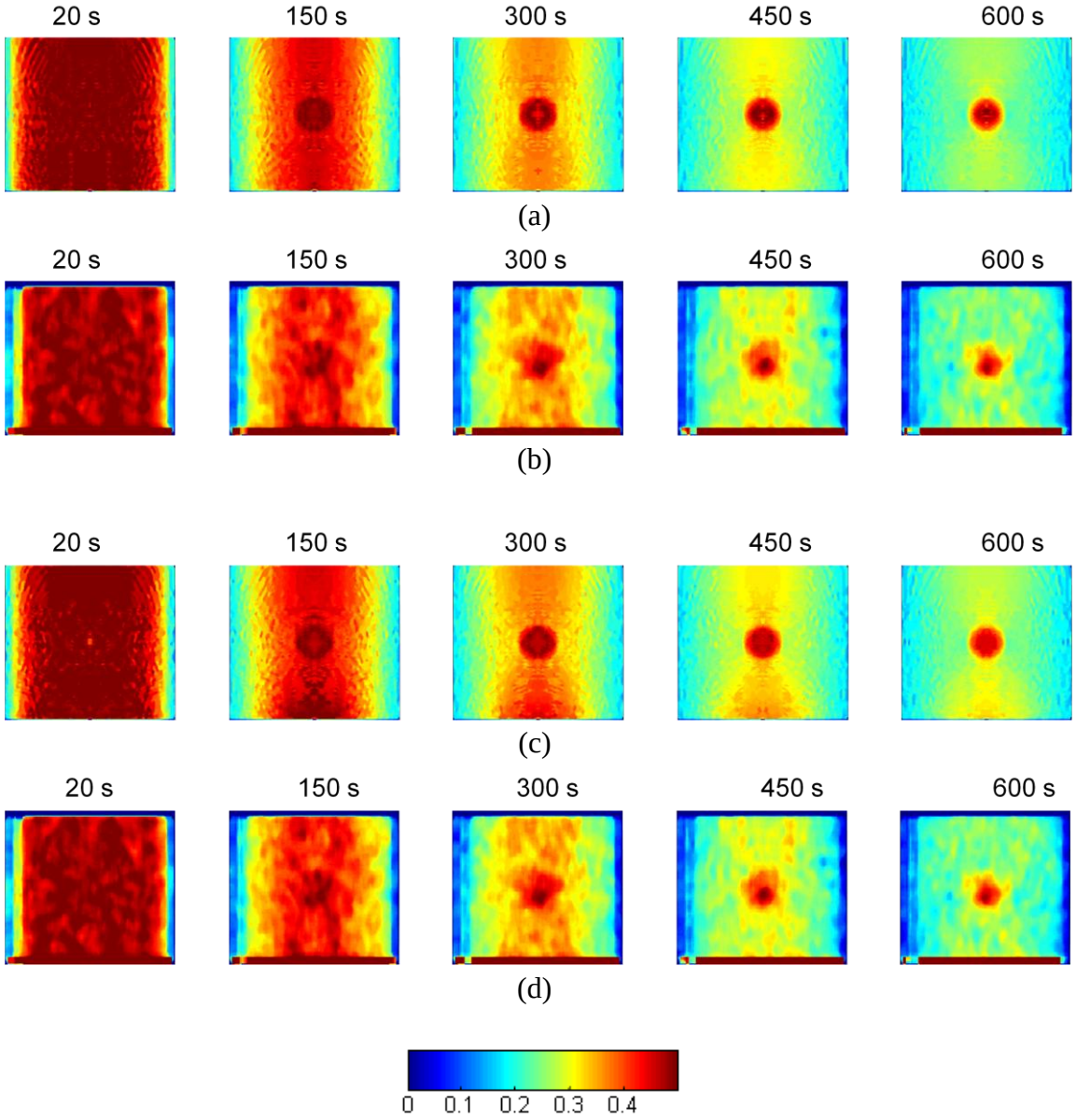


Figure 13.Time-sequenced EPR images for -20db permeability contrast between inclusion and background. (a) Ideal EPR maps and (b) corresponding EPR poroelastogram obtained under SR (c). Ideal EPR maps and (d) corresponding EPR poroelastogram obtained under creep compression. In each case images are displayed for time values equal to 20s, 150s ,300s and 600s as indicated in the figure.

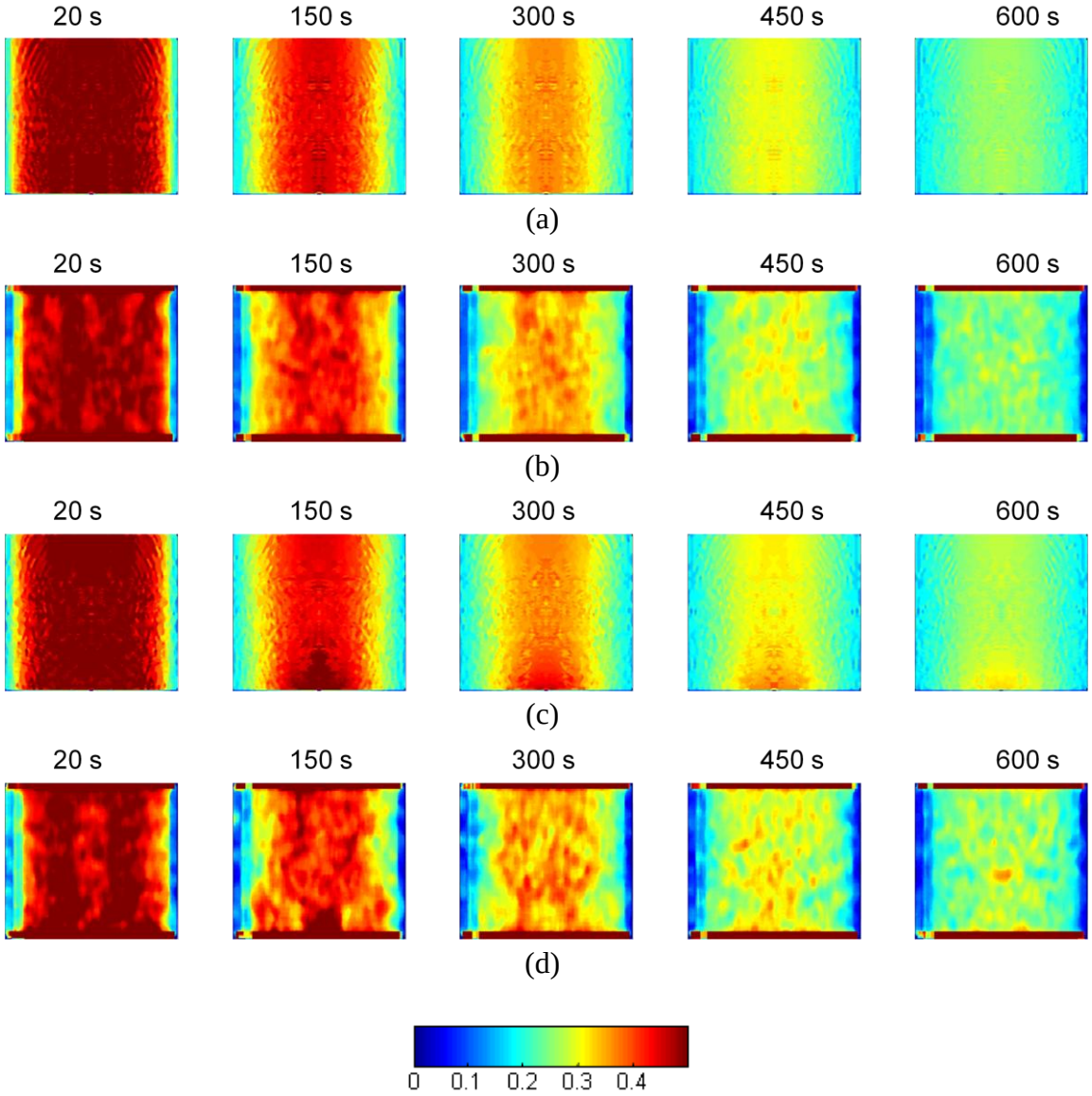


Figure 14.Time-sequenced EPR images for +20db permeability contrast between inclusion and background. (a) Ideal EPR maps and (b) corresponding EPR poroelastogram obtained under SR (c). Ideal EPR maps and (d) corresponding EPR poroelastogram obtained under creep compression. In each case images are displayed for time values equal to 20s, 150s ,300s and 600s as indicated in the figure.

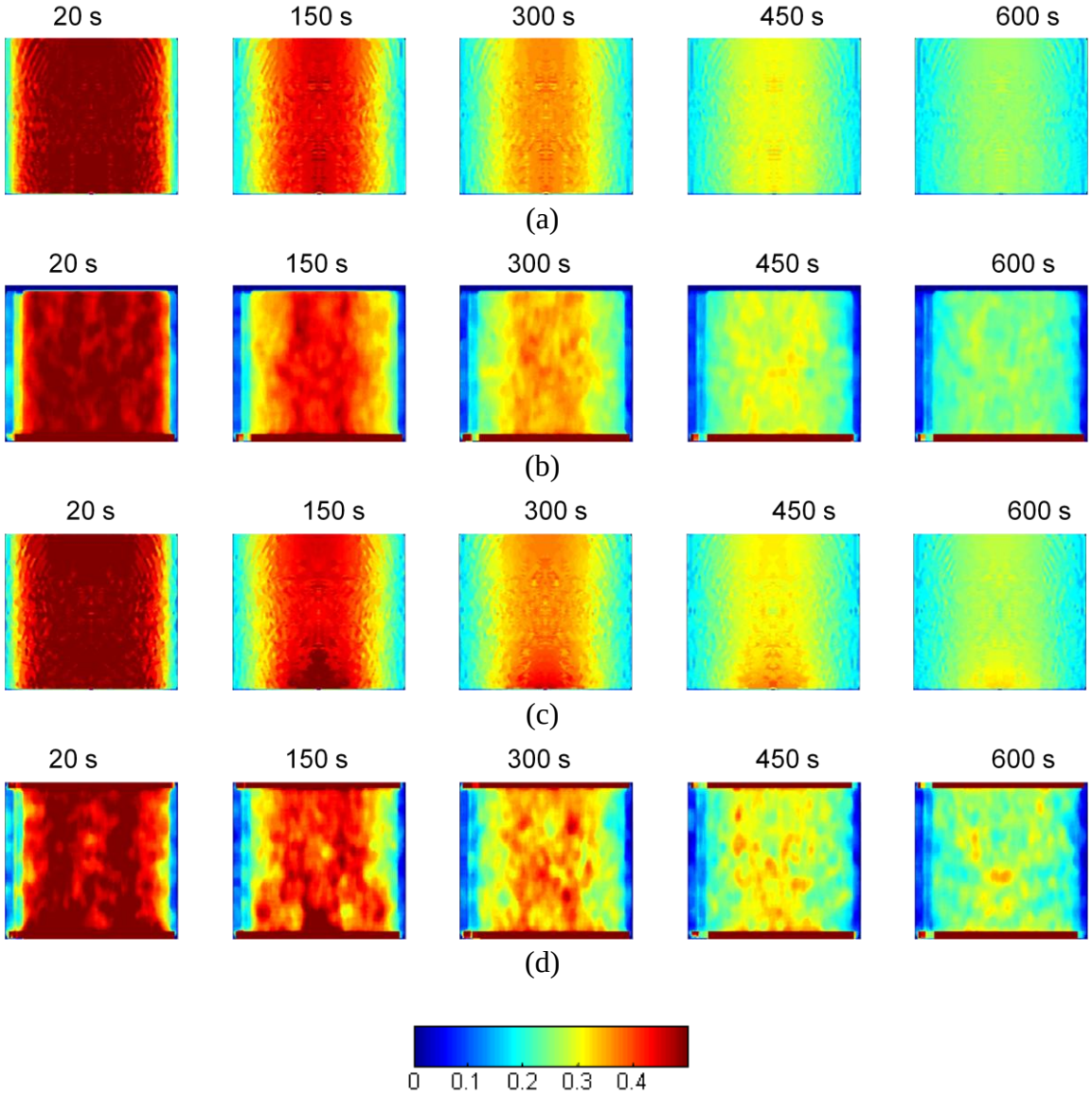


Figure 15. Time-sequenced EPR images for +40db permeability contrast between inclusion and background. (a) Ideal EPR maps and (b) corresponding EPR poroelastogram obtained under SR (c). Ideal EPR maps and (d) corresponding EPR poroelastogram obtained under creep compression. In each case images are displayed for time values equal to 20s, 150s ,300s and 600s as indicated in the figure.

*CNRe analysis for EPR poroelastograms (PCNRe)*

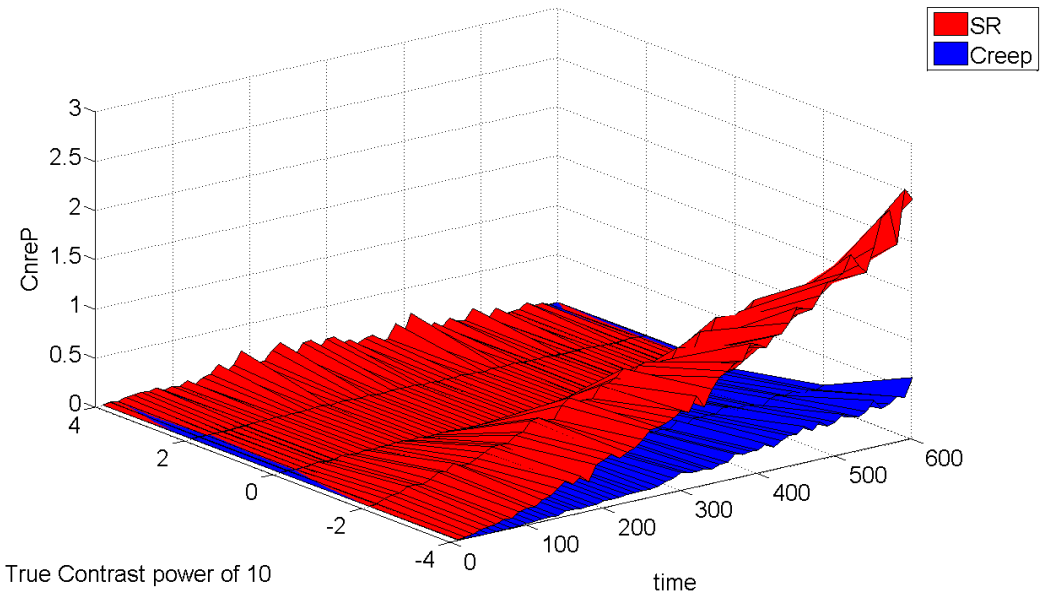


Fig 16. PCNRe plot for SR (red) and creep (blue).

Figure 16 shows the PCNRe as a function of time and underlying permeability contrast for the two compression techniques considered in this study. It can be observed that PCNRe is almost zero for all cases where the background is less permeable than the inclusion. In these cases the phantom behaves like a homogeneous poroelastic material because fluid exudation from the inclusion is constrained by the surrounding background material. For the reverse cases, i.e., a background more permeable than the inclusion, PCNRe improves with time especially in the case that the SR loading conditions is used.

*EPR poroelastogram accuracy analysis for permeability contrast*

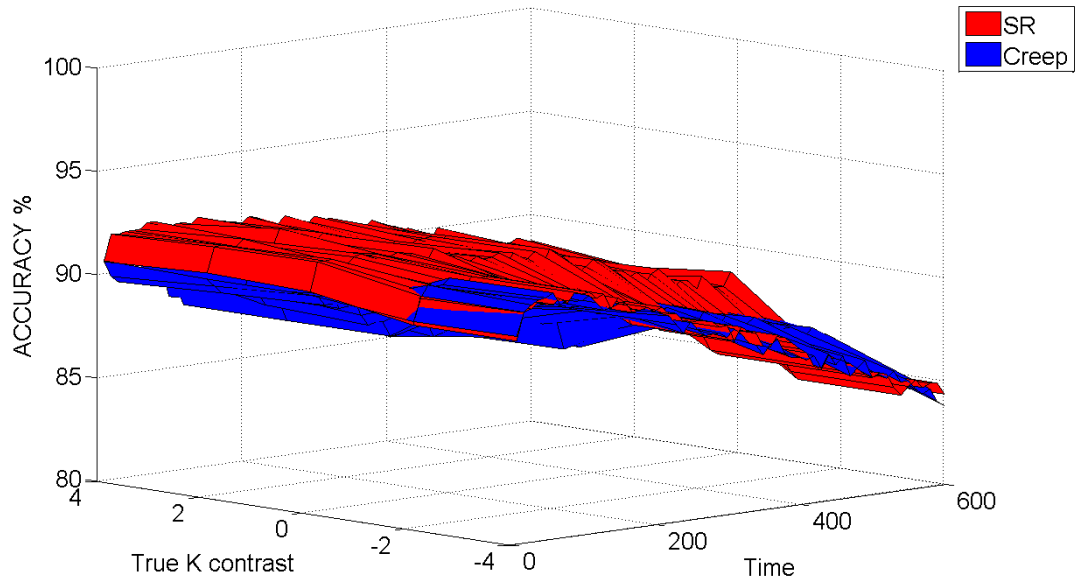


Fig 17. Accuracy plot of EPR poroelastograms.

From Figure 11 and Figure 17 it can be seen that accuracy for EPR poroelastograms is significantly lower than the axial strain case. This is expected given the well known image quality limitations of EPR elastography with respect to axial strain elastography (Righetti et al. 2007b). However, overall, accuracy of EPR was still found > 80%. As opposed to the axial strain case, accuracy of EPR appears to decrease with time.

*Contrast Transfer Efficiency (CTE)*

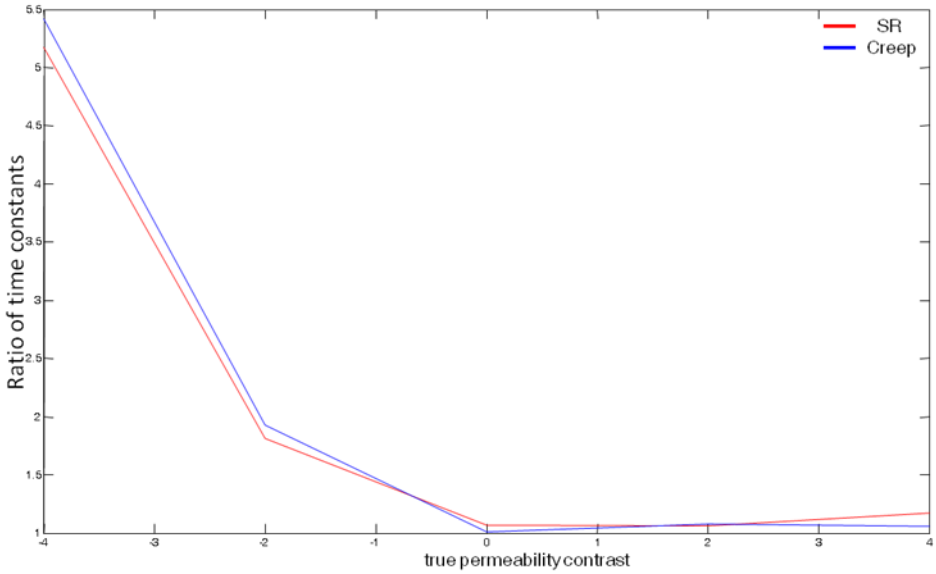


Fig 18. EPR CTE plot for permeability contrast.

*Discussion of the presented results*

The figures shown so far refer to the simulated mechanical models where only a permeability contrast between the background and the inclusion exist, while background and inclusion are assumed to have the exact same Young's modulus or Poisson's ratio contrast. Thus, any observed poroelastographic contrast should be attributed to the different rate of fluid clearance in the background and in the conclusion. A few important conclusions can be drawn from these results. First, the presence of an underlying permeability contrast can in general cause spatial and temporal changes in

both the axial strain and the EPR distributions. Second, the two cases – background *more* permeable than the inclusion and background *less* permeable than the inclusion - affect poroelastographic parameters and quality factors in a non-symmetric fashion. Following, I address these two cases separately.

*Background more permeable than inclusion*

In this case, the permeability of the inclusion is lower than the permeability of the background. Hence, under sustained compression, fluid inside the background moves at a faster rate with respect to the fluid inside the inclusion. Depending on the simulated permeability value, fluid flow inside the inclusion can be considered almost negligible within the chosen temporal window of observation. So, the poroelastographic parameters appear to be almost constant in time in the region corresponding to the inclusion. On the other hand, fluid in the background is free to flow outwards at a much faster rate, which creates a poroelastographic contrast visible in the axial strain poroelastograms. The EPR poroelastograms depict the same condition, where the EPR of the background decays quicker to the Poisson's ratio of the underlying matrix (drained condition). Due to its low permeability, the inclusion does not reach the drained condition in our window of observation. Hence even though the simulated Poisson's ratios of the matrix and of the inclusion are exactly the same, in the drained condition the EPR elastograms do not appear as uniform images.

The CNRe analysis shows that the CNRe is a function of time and improves with increasing underlying permeability contrast. Comparing the SR and creep results, we observe a crossover point at around 350 s after which SR method appears to have a

better performance over creep. Finally from Figure 18 it can be seen that CTE for this case shows a non linear dependence with respect to the underlying contrast.

*Inclusion is more permeable than background*

In this case, the permeability of the background is lower than the permeability of the inclusion. Hence, under compression, fluid inside the inclusion is constrained by the surrounding background. So, the fluid flow rate in the background controls the fluid movement in the entire medium. Effectively, the medium behaves like a homogeneous poroelastic material. Since there is no other contrast than the permeability contrast, CNRe, PCNRe and CTE values for these cases are practically zero (not shown).

**3. Young's modulus contrast**

The following results were obtained by varying the Young's modulus contrast between the background solid matrix and the inclusion solid matrix from 10^-2to 10^2 i.e. from -20db to +20db. No permeability or Poisson's ratio contrast was simulated for these results.

Figures 19-22 show the axial strain poroelastograms along with the corresponding ideal axial strain maps.

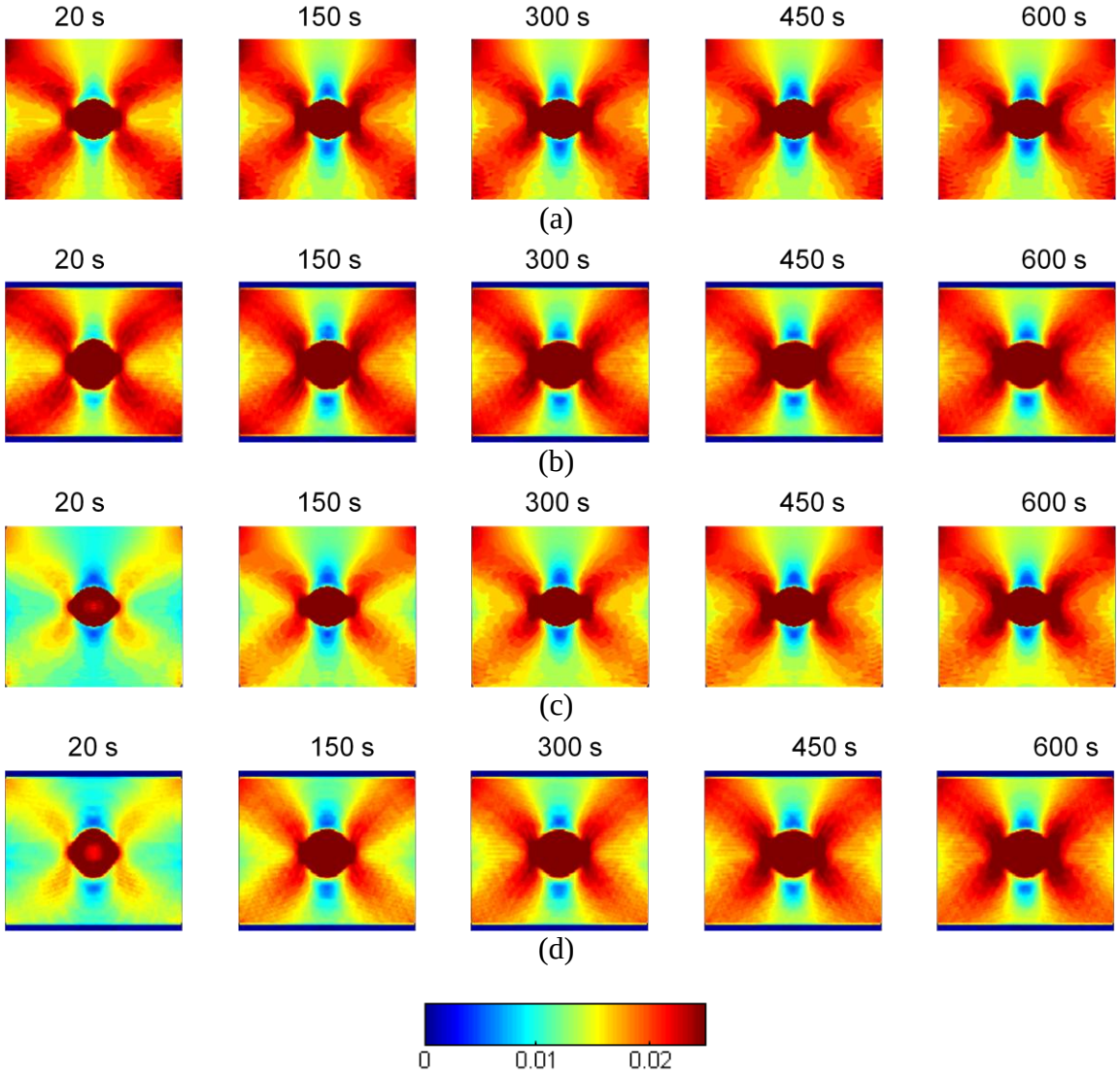


Figure 19. Time-sequenced axial strain images for -20db Young's modulus contrast between inclusion and background. (a) Ideal axial strain maps obtained simulating SR loading (b) Axial strain poroelastogram obtained simulating SR loading (c) Ideal axial strain maps obtained simulating creep loading (d) Axial strain poroelastogram obtained simulating creep loading. In each case images are displayed for time values equal to 20s, 150s ,300s and 600s respectively.

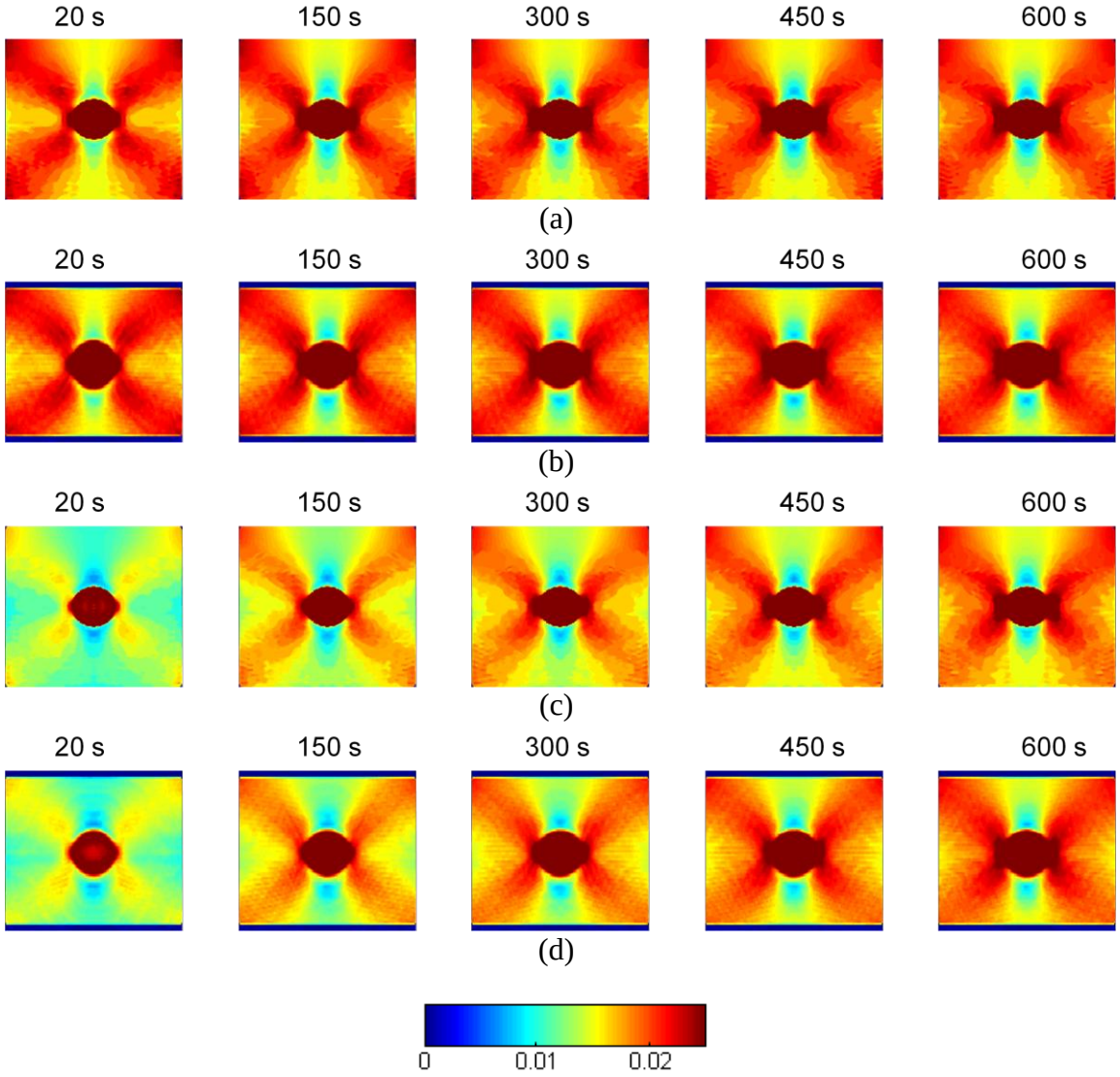


Figure 20. Time-sequenced axial strain images for -10 db Young's modulus contrast between inclusion and background. (a) Ideal axial strain maps obtained simulating SR loading (b) Axial strain poroelastogram obtained simulating SR loading (c) Ideal axial strain maps obtained simulating creep loading (d) Axial strain poroelastogram obtained simulating creep loading. In each case images are displayed for time values equal to 20s, 150s ,300s and 600s as indicated in the figure.

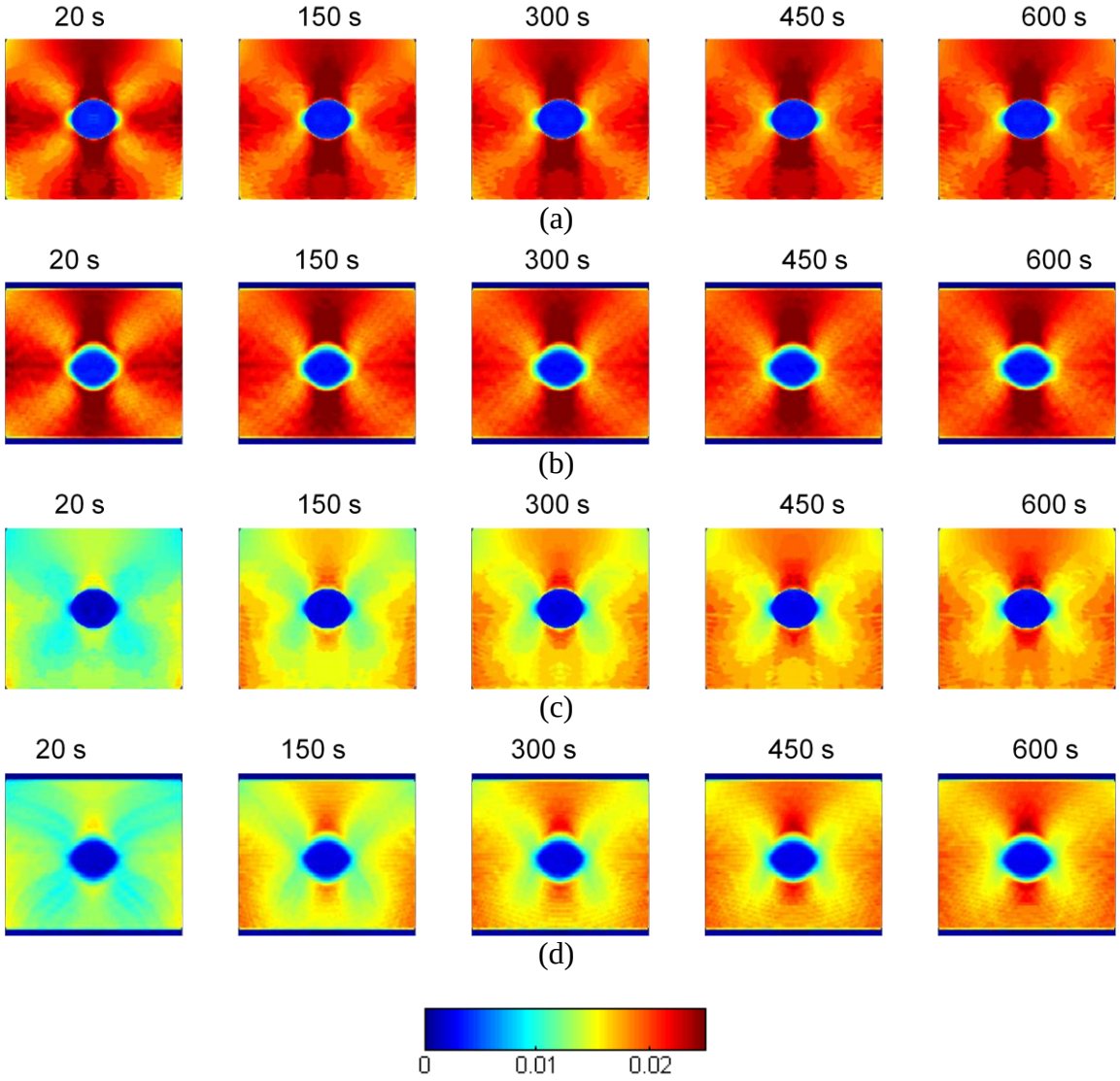


Figure 21.Time-sequenced axial strain images for +10db Young's modulus contrast between inclusion and background. (a) Ideal axial strain maps obtained simulating SR loading (b) Axial strain poroelastogram obtained simulating SR loading (c) Ideal axial strain maps obtained simulating creep loading (d) Axial strain poroelastogram obtained simulating creep loading. In each case images are displayed for time values equal to 20s, 150s ,300s and 600s as indicated in the figure.

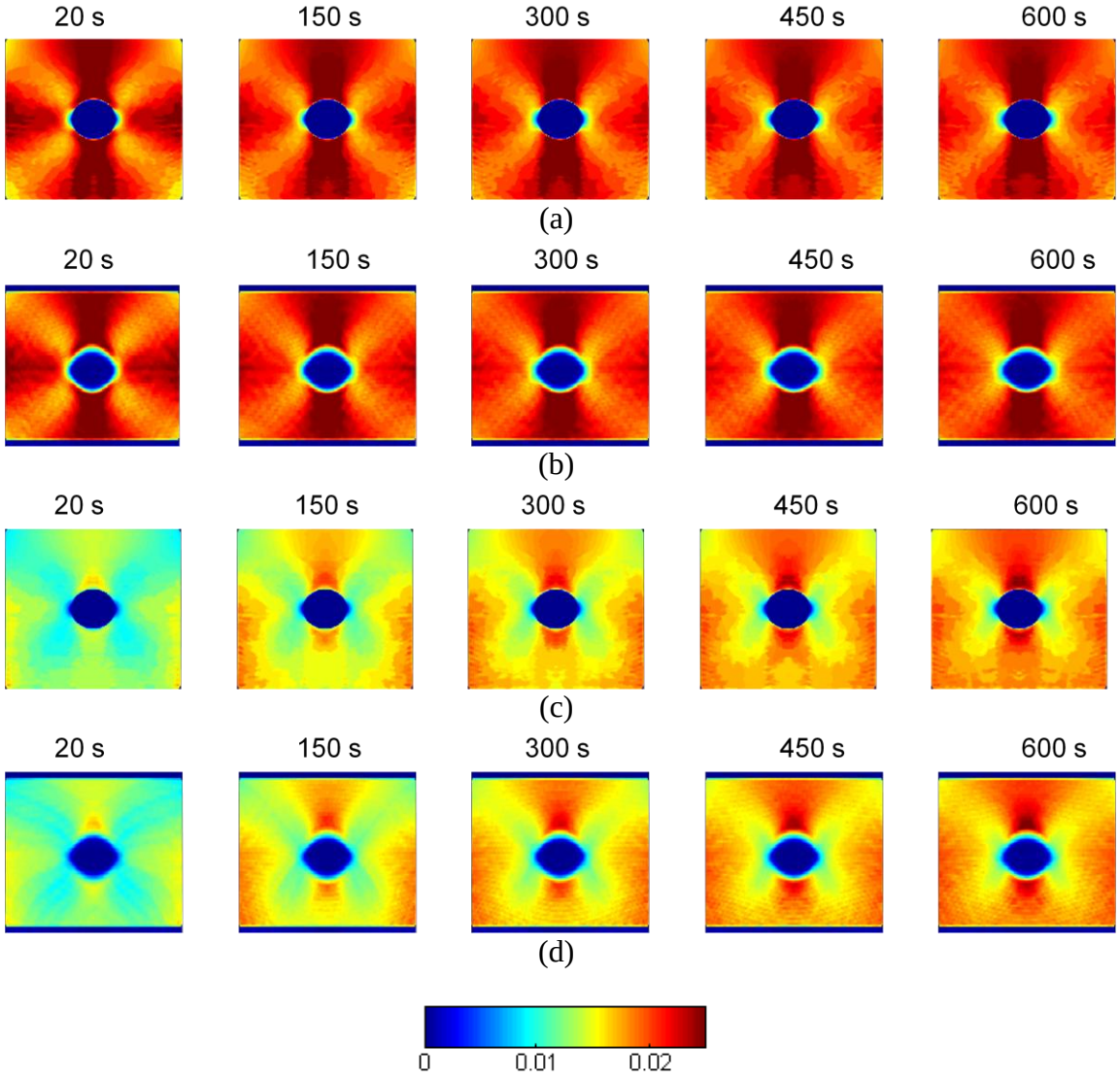


Figure 22.Time-sequenced axial strain images for +20db Young's modulus contrast between inclusion and background. (a) Ideal axial strain maps obtained simulating SR loading (b) Axial strain poroelastogram obtained simulating SR loading (c) Ideal axial strain maps obtained simulating creep loading (d) Axial strain poroelastogram obtained simulating creep loading. In each case images are displayed for time values equal to 20s, 150s ,300s and 600s as indicated in the figure.

*Young's modulus contrast CNRe analysis for axial strain poroelastograms*

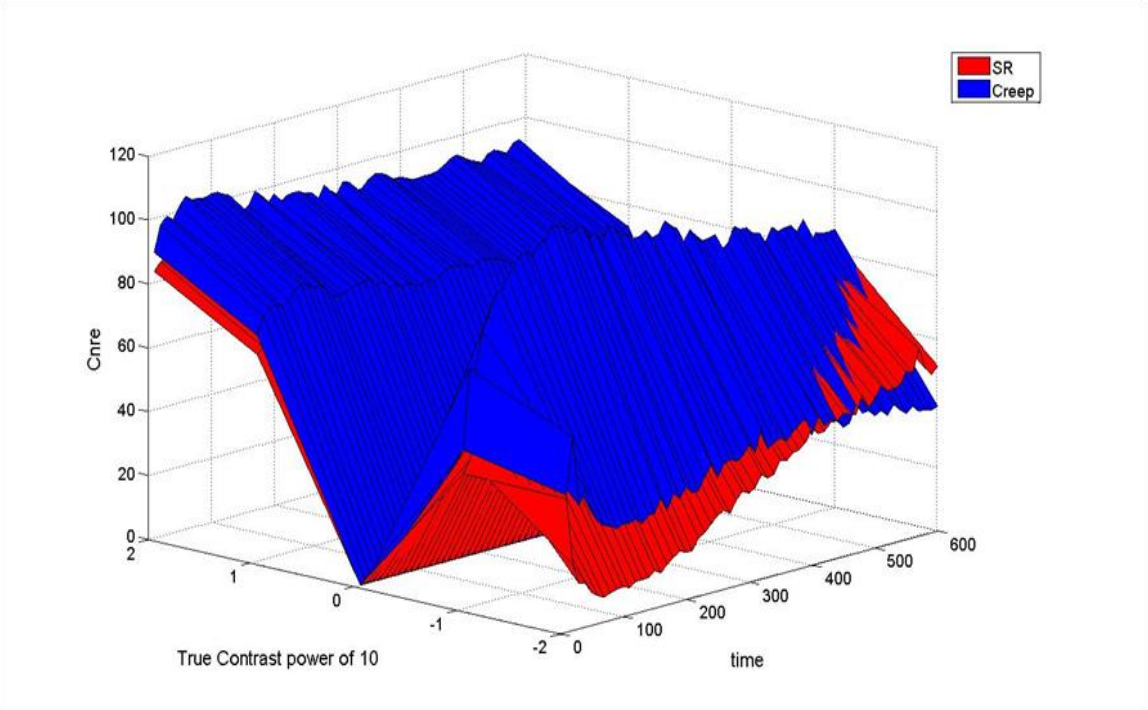


Fig 23. Young's modulus contrast CNRe for axial strain poroelastograms

Figure 23 shows a three dimensional plot of the axial strain CNRe as a function of time and true Young's modulus contrast..CNRe for low Young's modulus contrast, CNRe values are similar whether you have an inclusion stiffer or softer than the background. However, for high Young's modulus contrast, CNRe is significantly higher for the case of a stiffer inclusion in a softer background that the reverse case. These findings confirm previous elastography findings (Ponnekanti et al. 1995).Figure 24 to Figure 27 show the statistical comparison of CNRe for this case and Figure 28 shows the accuracy plot .

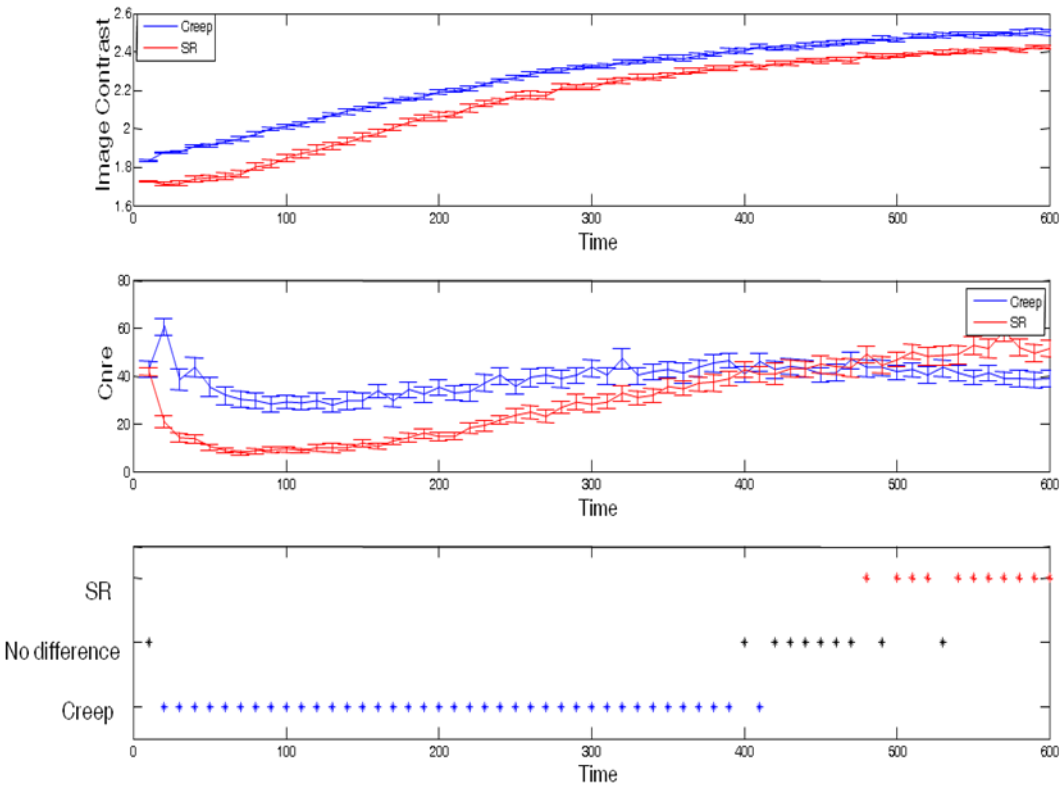


Figure 24. Statistical comparison between CNRe obtained with SR and CNRe obtained with creep for -20db Young's modulus contrast between inclusion and background.From top to bottom : Image contrast as a function of time for SR (red) and creep(blue) (error bars represent 95% confidence interval), CNRe as a function of time for SR (red) and creep(blue) (error bars represent 95% confidence interval) and statistical comparison of the two compression techniques .

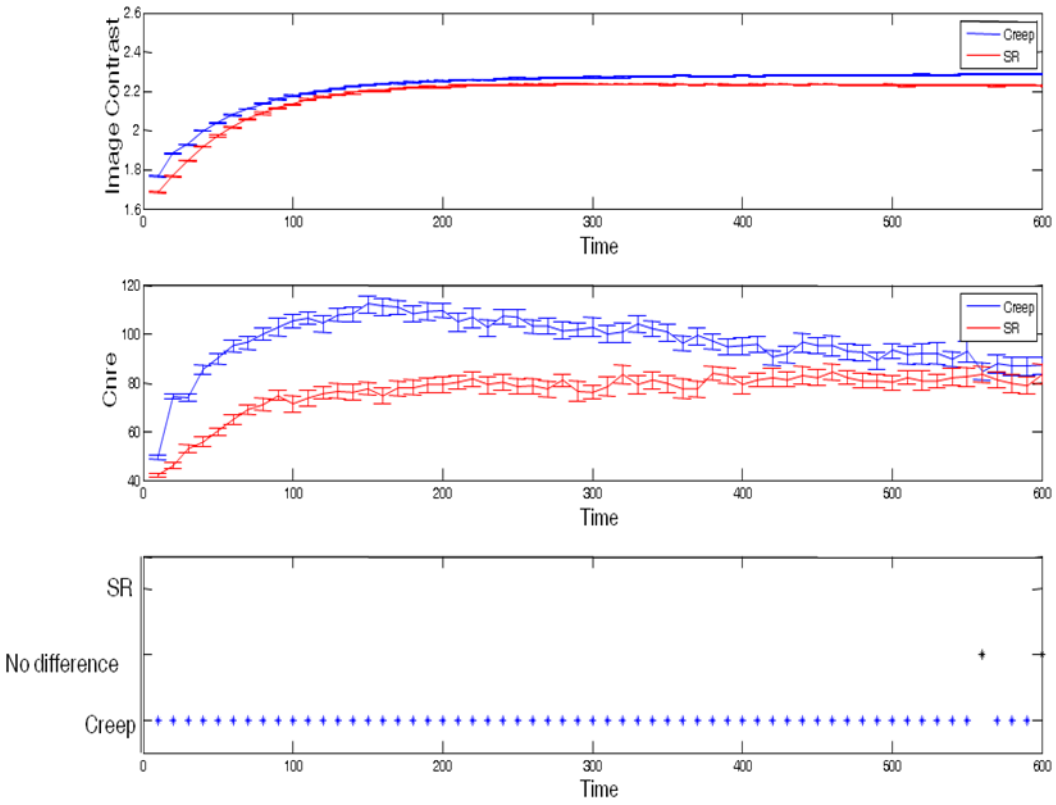


Figure 25. Statistical comparison between CNRe obtained with SR and CNRe obtained with creep for -10db Young's modulus contrast between inclusion and background.From top to bottom : Image contrast as a function of time for SR (red) and creep(blue) (error bars represent 95% confidence interval), CNRe as a function of time for SR (red) and creep(blue) (error bars represent 95% confidence interval) and statistical comparison of the two compression techniques .

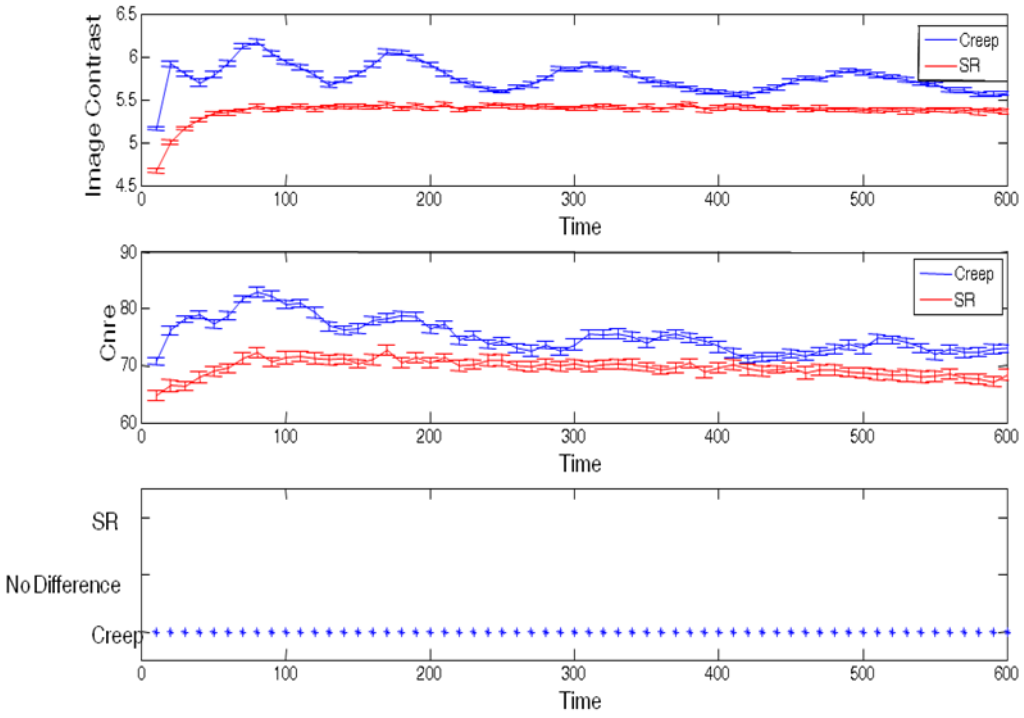


Figure 26. Statistical comparison between CNRe obtained with SR and CNRe obtained with creep for +10db Young's modulus contrast between inclusion and background. From top to bottom: Image contrast as a function of time for SR (red) and creep(blue) (error bars represent 95% confidence interval), CNRe as a function of time for SR (red) and creep(blue) (error bars represent 95% confidence interval) and statistical comparison of the two compression techniques .

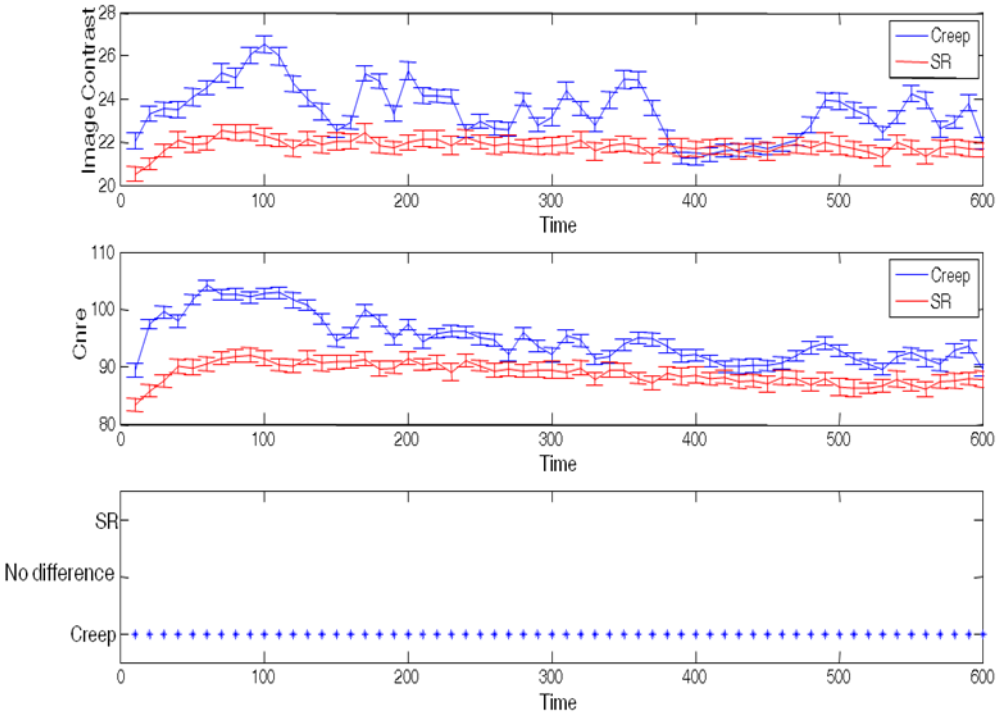


Figure 27. Statistical comparison between CNRe obtained with SR and CNRe obtained with creep for +20db Young's modulus contrast between inclusion and background. From top to bottom : Image contrast as a function of time for SR (red) and creep(blue) (error bars represent 95% confidence interval), CNRe as a function of time for SR (red) and creep(blue) (error bars represent 95% confidence interval) and statistical comparison of the two compression techniques .

*Young's modulus contrast accuracy analysis*

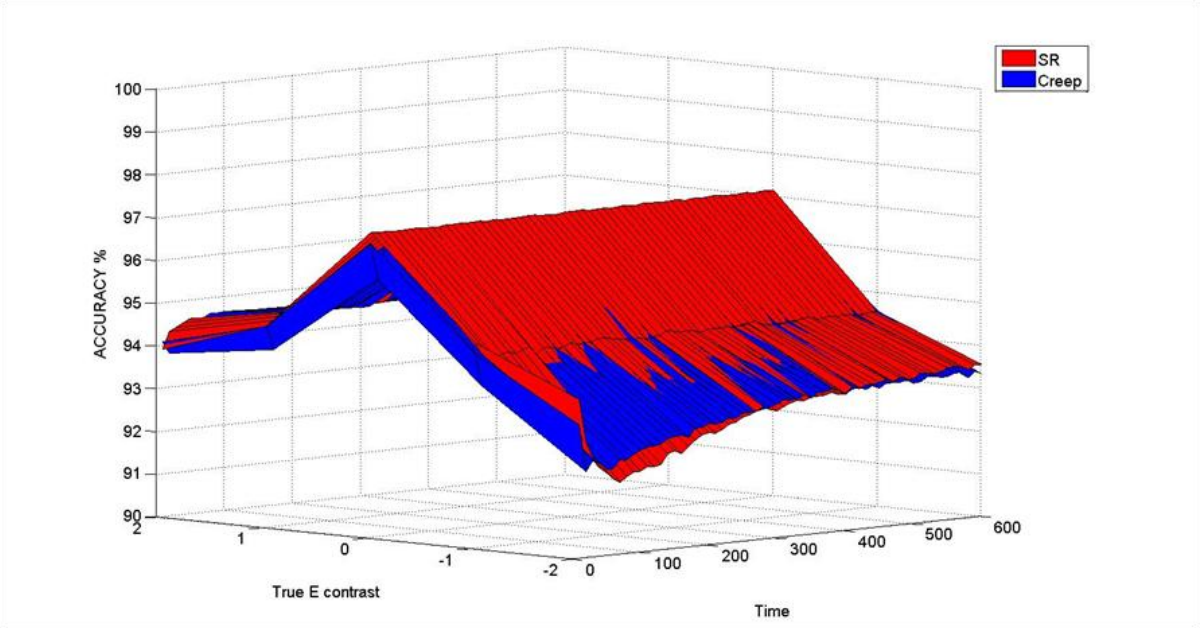


Fig 28. Young's modulus accuracy plot.

*Effective Poisson's Ratio (EPR) poroelastography*

Figures 29-33 show the EPR poroelastograms for the Young's modulus contrast along with the corresponding ideal images.

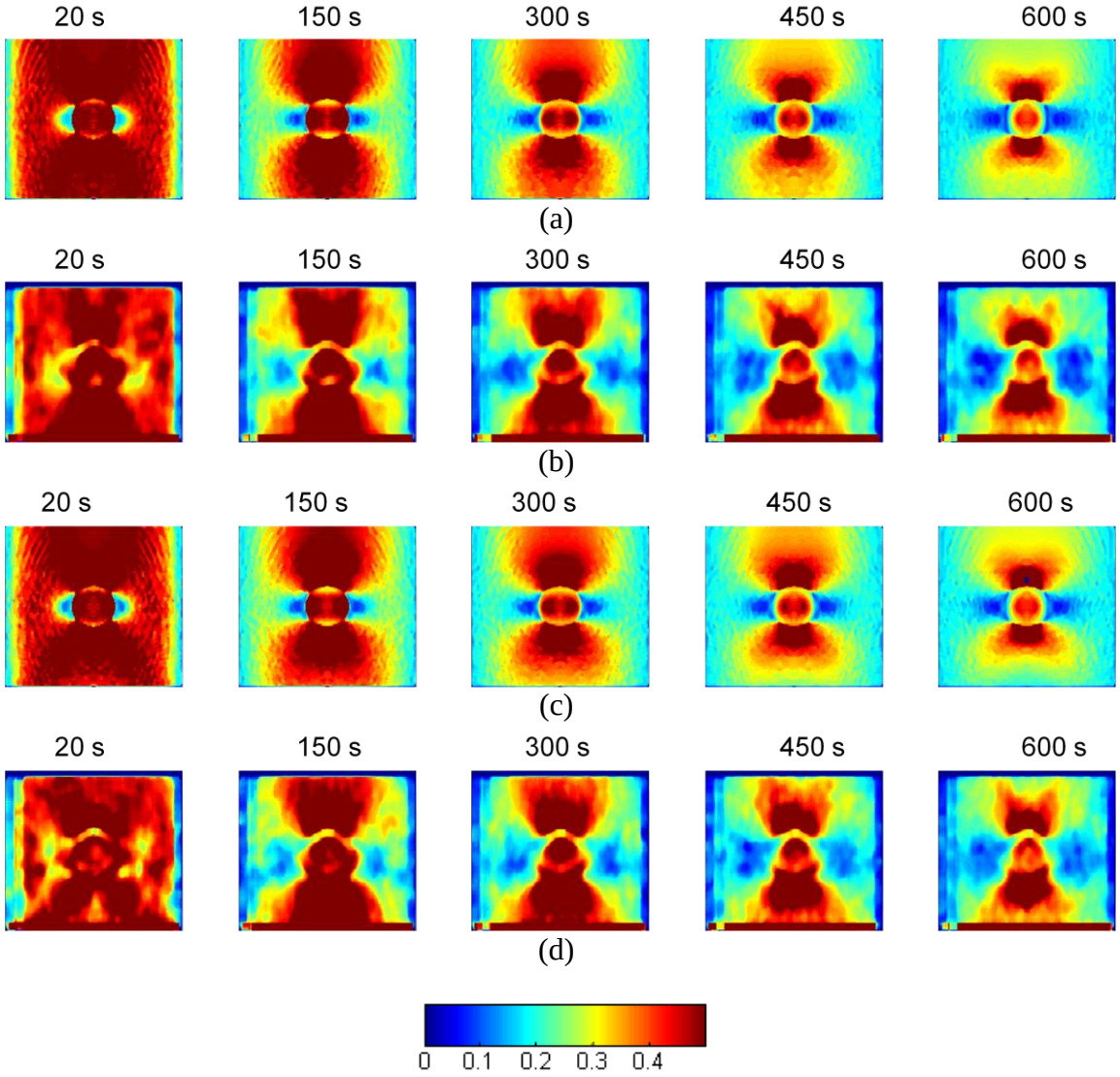


Figure 29. Time-sequenced EPR images for -20db Young's modulus contrast between inclusion and background. (a) Ideal EPR maps obtained simulating SR loading (b) EPR poroelastogram obtained simulating SR loading (c) Ideal EPR maps obtained simulating creep loading (d) EPR poroelastogram obtained simulating creep loading. In each case images are displayed for time values equal to 20s, 150s ,300s and 600s as indicated in the figure.

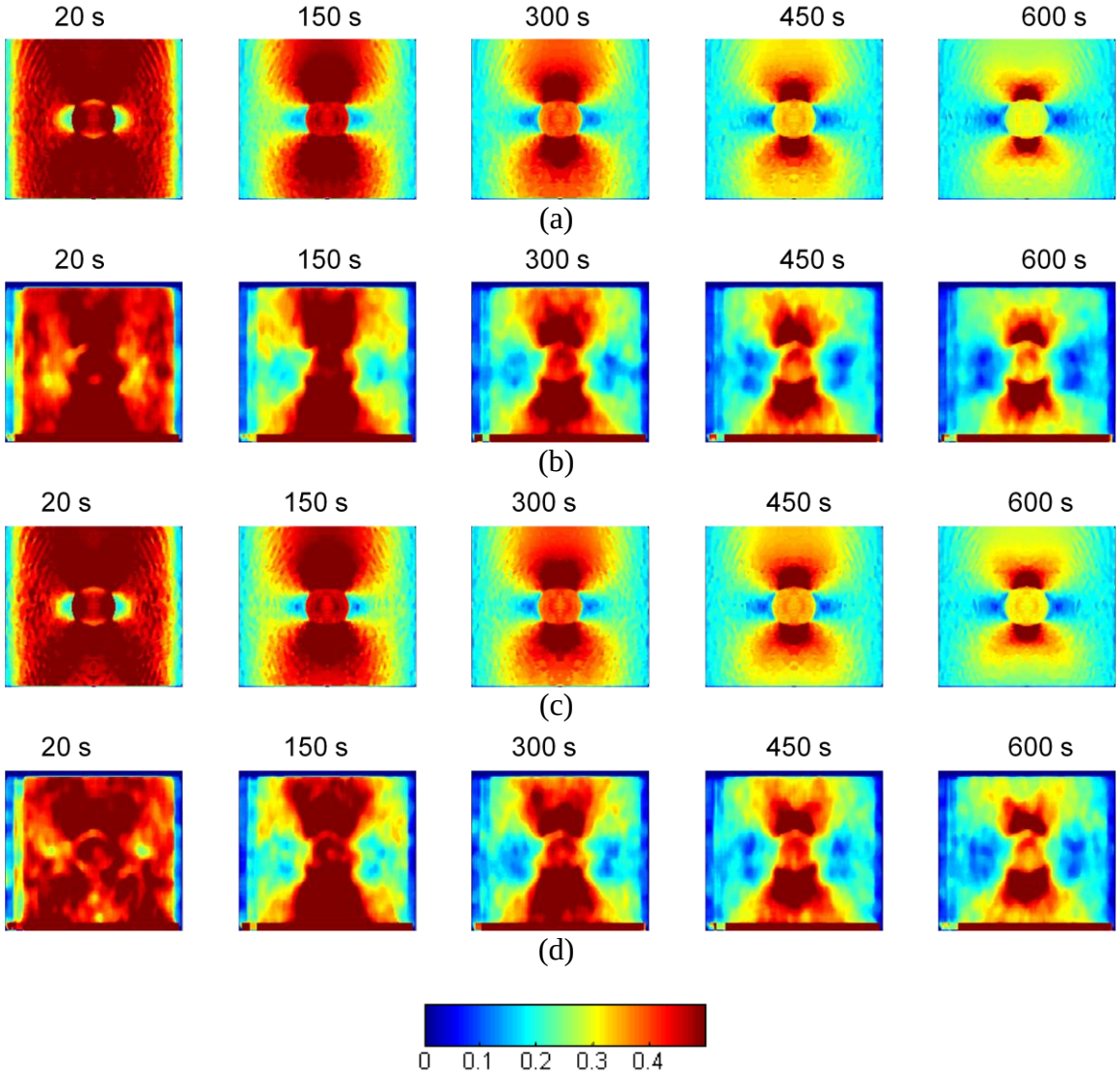


Figure 30. Time-sequenced EPR images for -10db Young's modulus contrast between inclusion and background. (a) Ideal EPR maps obtained simulating SR loading (b) EPR poroelastogram obtained simulating SR loading (c) Ideal EPR maps obtained simulating creep loading (d) EPR poroelastogram obtained simulating creep loading. In each case images are displayed for time values equal to 20s, 150s ,300s and 600s as indicated in the figure.

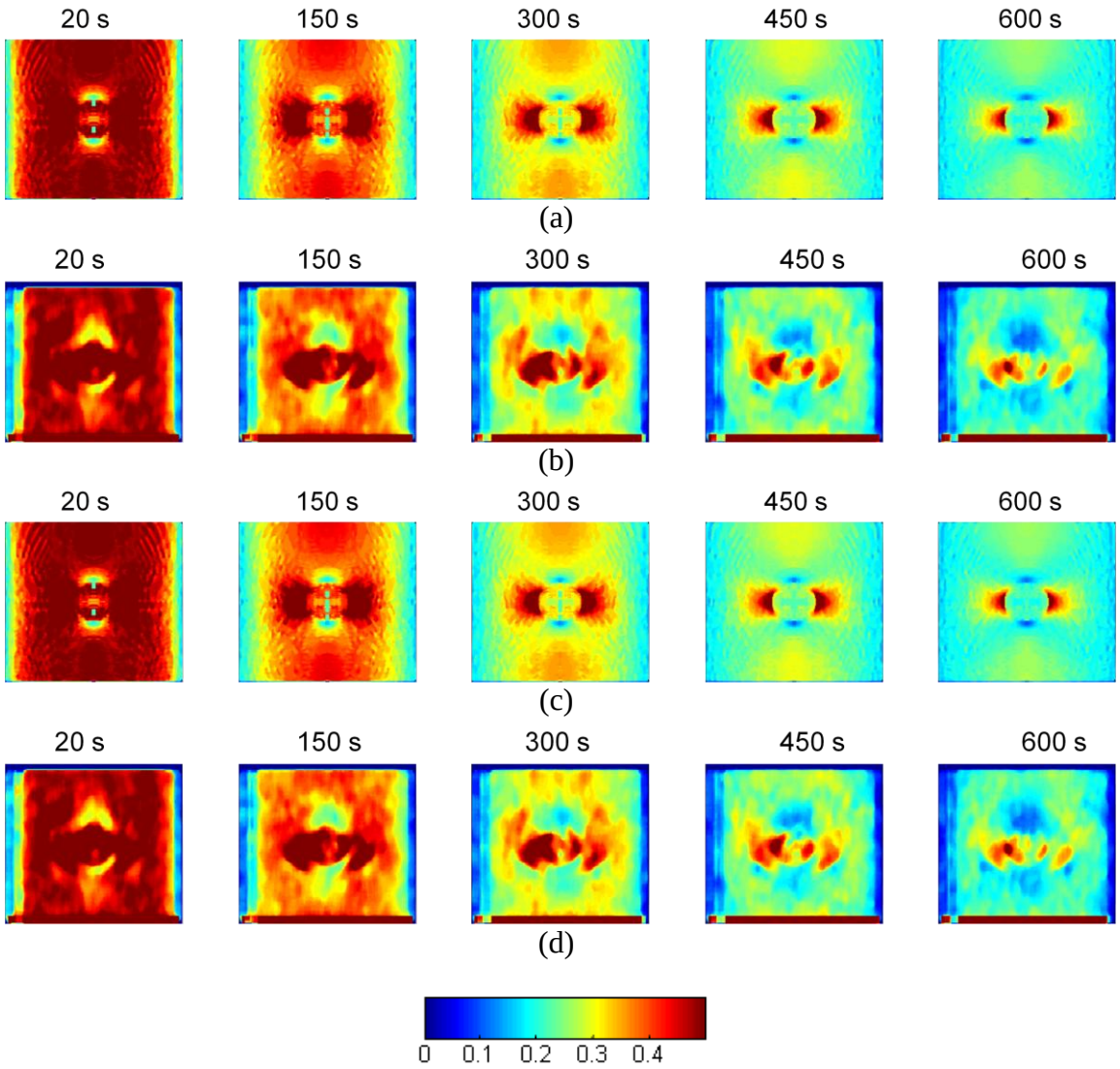


Figure 31. Time-sequenced EPR images for +10db Young's modulus contrast between inclusion and background. (a) Ideal EPR maps obtained simulating SR loading (b) EPR poroelastogram obtained simulating SR loading (c) Ideal EPR maps obtained simulating creep loading (d) EPR poroelastogram obtained simulating creep loading. In each case images are displayed for time values equal to 20s, 150s ,300s and 600s as indicated in the figure.

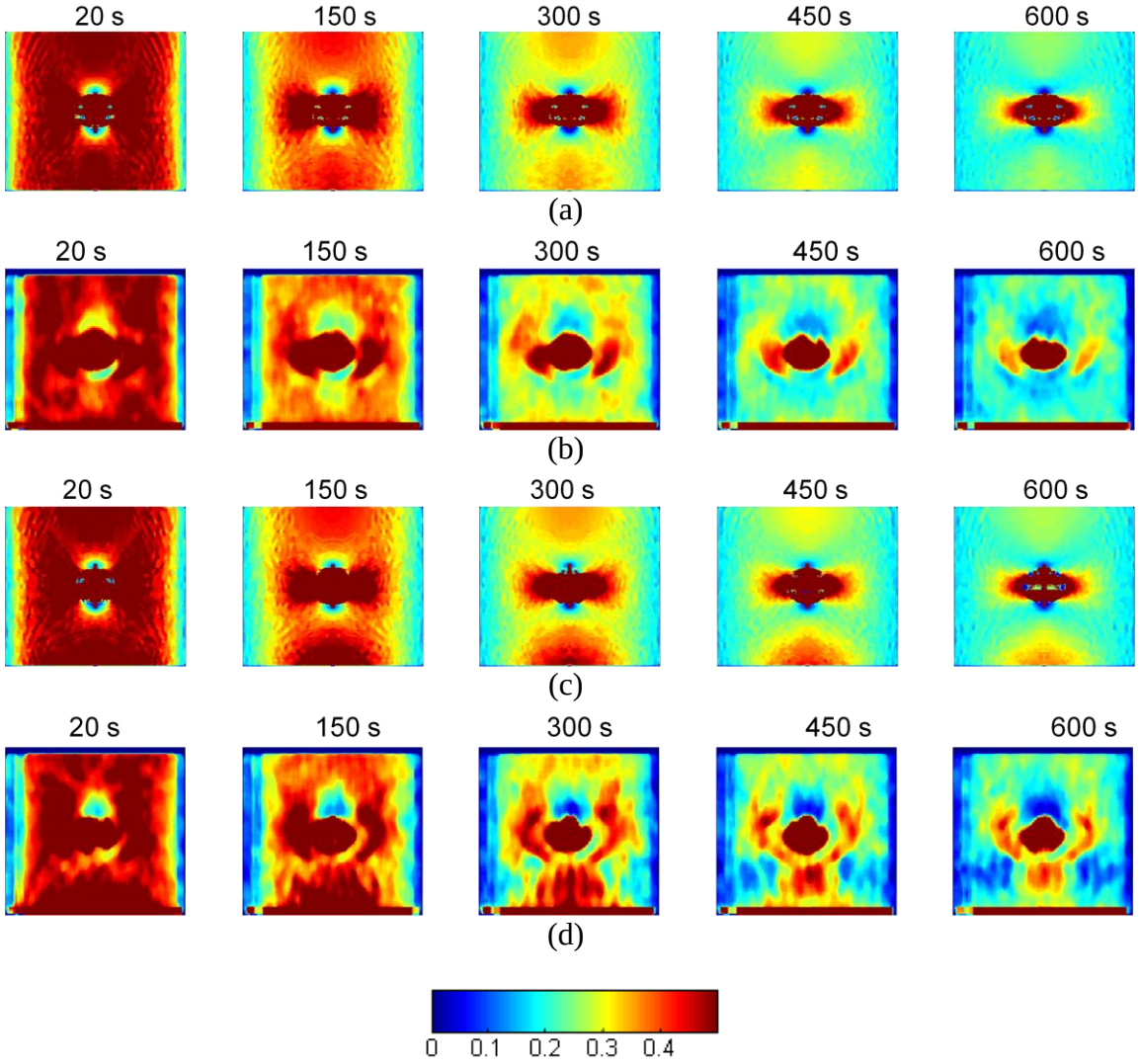


Figure 32. Time-sequenced EPR images for +20db Young's modulus contrast between inclusion and background. (a) Ideal EPR maps obtained simulating SR loading (b) EPR poroelastogram obtained simulating SR loading (c) Ideal EPR maps obtained simulating creep loading (d) EPR poroelastogram obtained simulating creep loading. In each case images are displayed for time values equal to 20s, 150s ,300s and 600s as indicated in the figure.

*Effective Poisson's ratio CNRe (PCNRe) analysis*

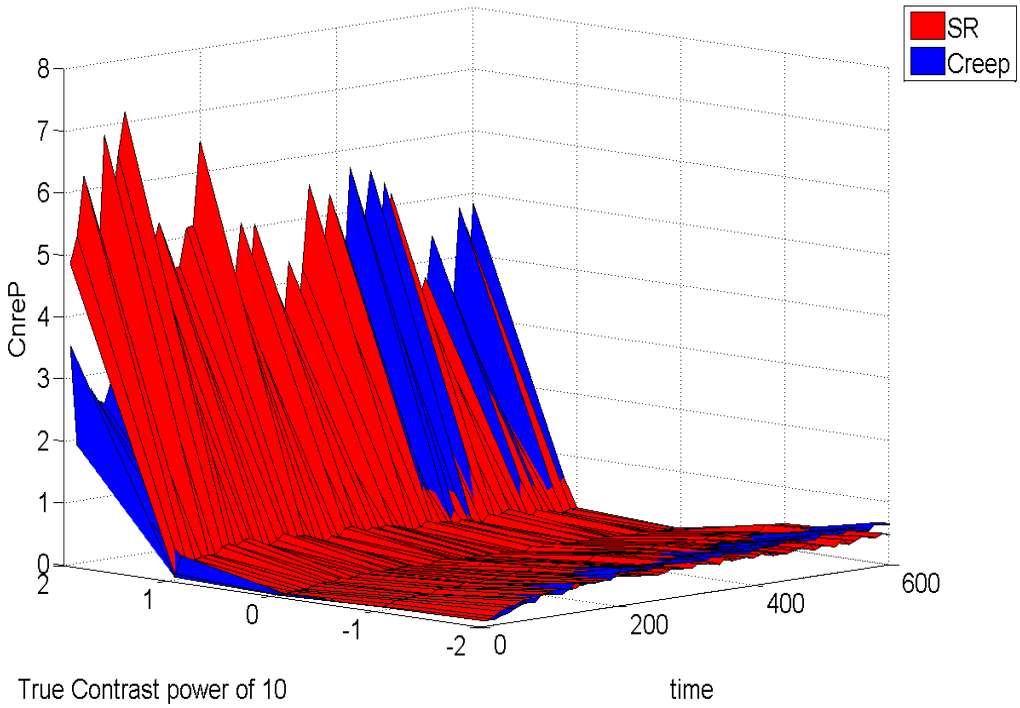


Fig 33 . PCNRe as a function of time and Young's modulus contrast.

*Young's modulus contrast EPR accuracy analysis*

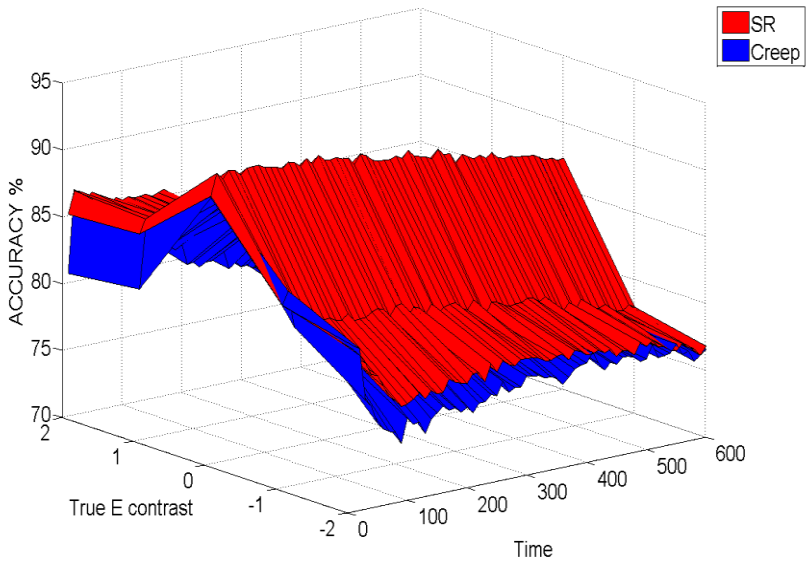


Fig 34. EPR accuracy plot as a function of time and Young's modulus contrast.

*Young's modulus contrast CTE*

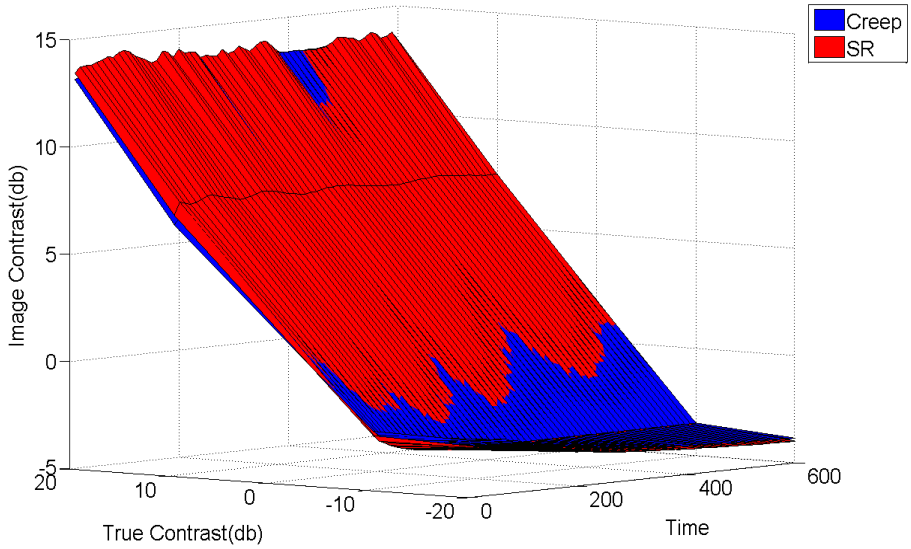


Fig 35. Young's modulus CTE plot.

*Discussion of the presented results*

From the presented results (Figure 34 and Figure 35), it is possible to infer that that the CNRe corresponding to a Young's modulus contrast is in general higher than in the case of a permeability contrast. The rate of fluid flow given by the time constant ($\tau$) through a poroelastic material is inversely proportional to the Young's modulus of the solid matrix (Armstrong et al. 1984). As in the case of the permeability contrast we see that the two cases of a hard inclusion in a soft background and a soft inclusion in a hard background have asymmetric effect on poroelastographic image quality.

*Soft inclusion in a hard background*

For the cases of a soft inclusion in a hard background i.e. $\tau_b<\tau_i$, fluid flow from the inclusion appears again to be restricted by that of the background .Due to the stiffness of the background, fluid does not drain completely from the material in our window of observation. Hence in the resulting poroelastograms the Poisson's ratio of the inclusion does not reach the undrained value.

*Soft inclusion in a hard background*

For this case $\tau_b > \tau_i$ , therefore fluid from background flows at a faster rate than the fluid inside the inclusion. For the +10db case the difference is small hence both background and inclusion reach the drained condition in our window of observation. However for +20db contrast $\tau_{i<<} \tau_b$ . In this case fluid flow in inclusion is very slow as compared to the background and does not reach the drained condition in out window of observation. Consequently, the PCNRe for this case is much higher than that of the other cases as shown in Figure 33. The CTE analysis confirms the well-known limitations of standard elastography methods in depicting Young's modulus contrasts when a soft inclusion is embedded in hard background (Ponekanti et al. 1995, Kallel et al. 1996). Differences in performances of the two compression techniques in terms of accuracy, CNRe , PCNRe and CTE are statistically significant with the creep leading to higher image quality factors for axial strain poroelastograms and SR for EPR poroelastograms.

**4. Poisson's ratio contrast**

Figures 36-37 show axial strain poroelastograms for an undrained Poisson's ratio contrast between background and inclusion of 1.8 and 0.2 respectively and Figure 38 shows the CNRe analysis plot for this case.

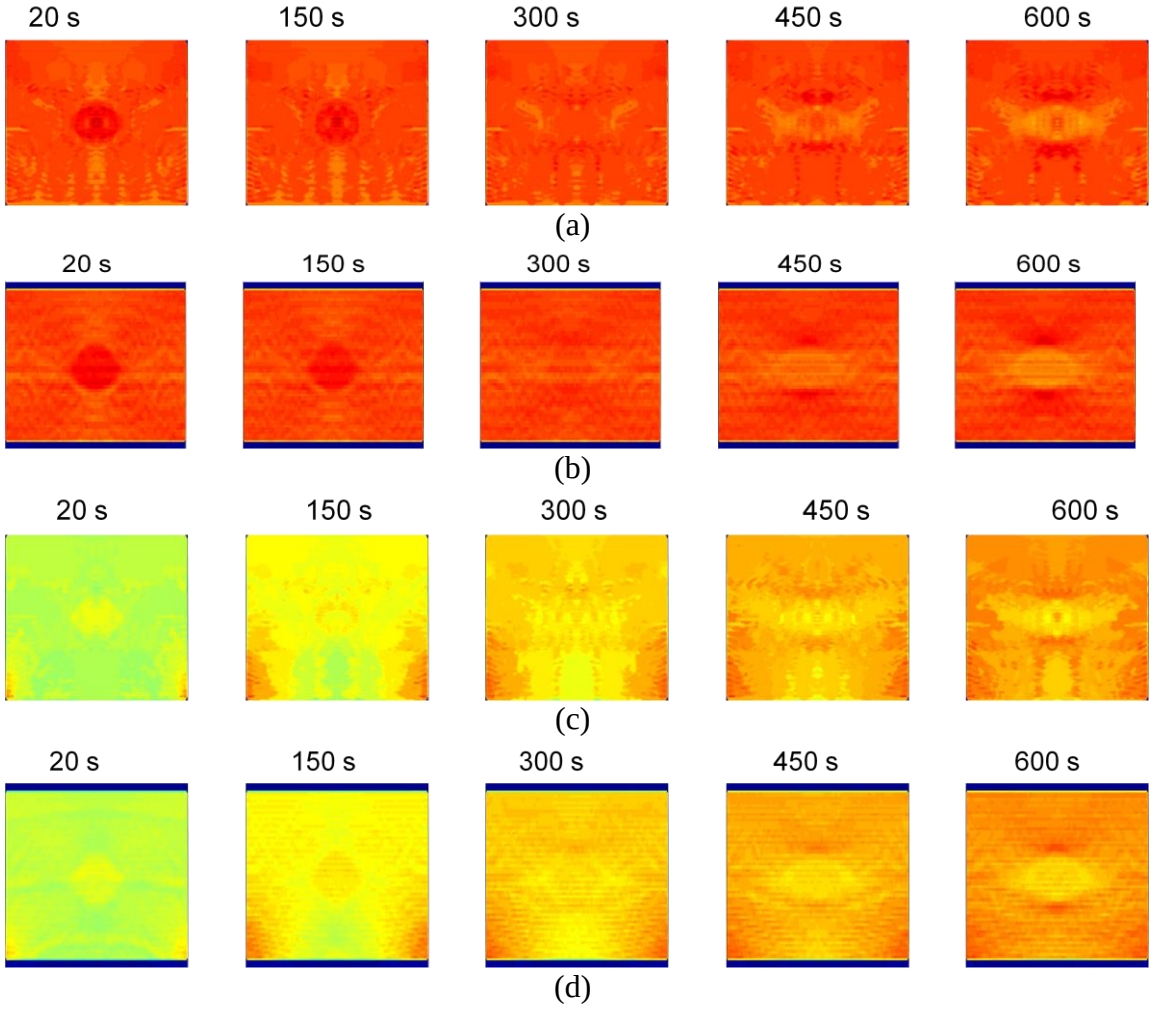


Figure 36. Time-sequenced axial strain images for 1.8 Poisson's ratio contrast between inclusion and background. (a) Ideal axial strain maps obtained simulating SR loading (b) axial strain poroelastogram obtained simulating SR loading (c) Ideal axial strain maps obtained simulating creep loading (d) axial strain poroelastogram obtained simulating creep loading. In each case images are displayed for time values equal to 20s, 150s ,300s and 600s respectively.

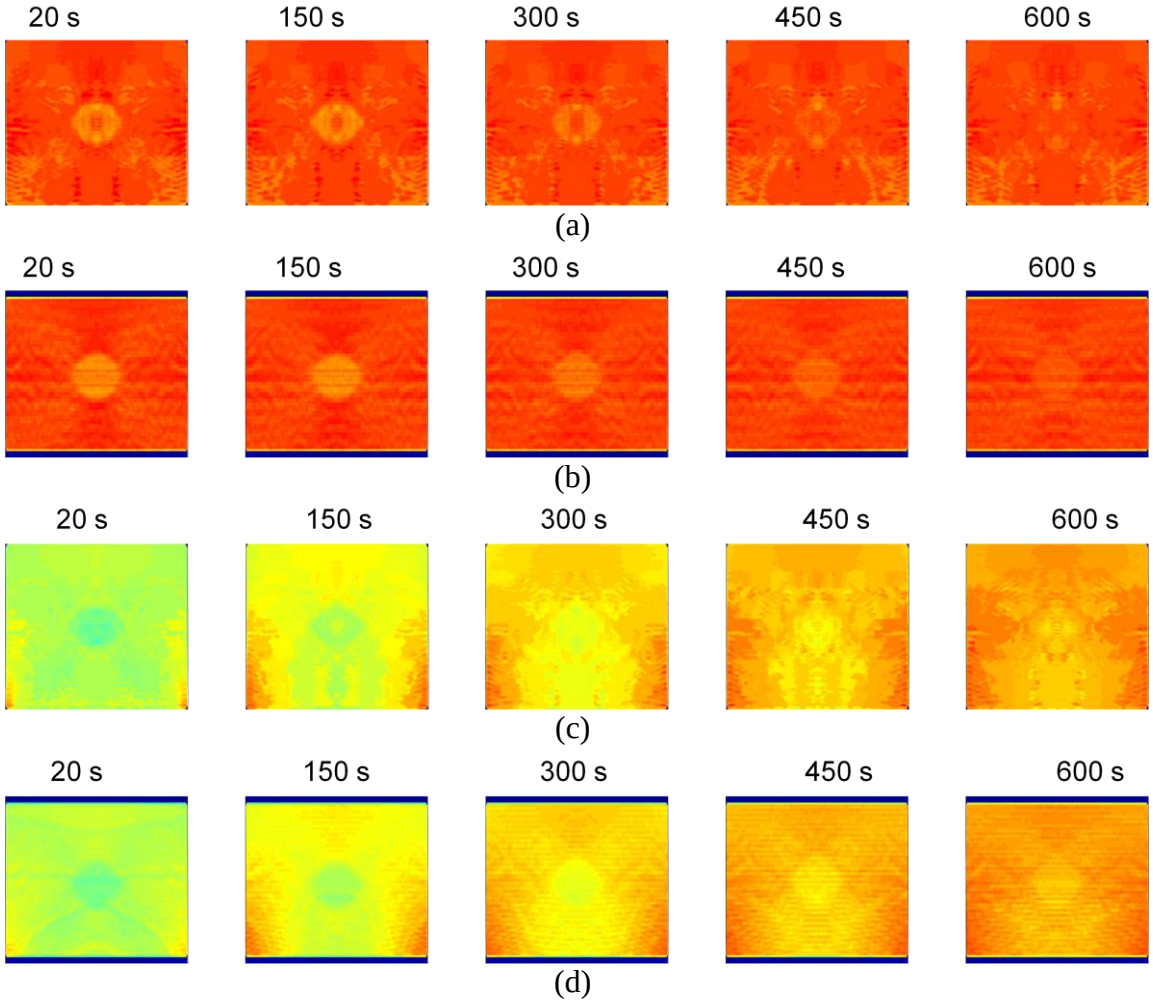


Figure 37. Time-sequenced axial strain images for 0.2 Poisson's ratio contrast between inclusion and background. (a) Ideal axial strain maps obtained simulating SR loading (b) axial strain poroelastogram obtained simulating SR loading (c) Ideal axial strain maps obtained simulating creep loading (d) axial strain poroelastogram obtained simulating creep loading. In each case images are displayed for time values equal to 20s, 150s ,300s and 600s as indicated in the figure.

*Poisson's ratio contrast axial strain CNRe analysis*

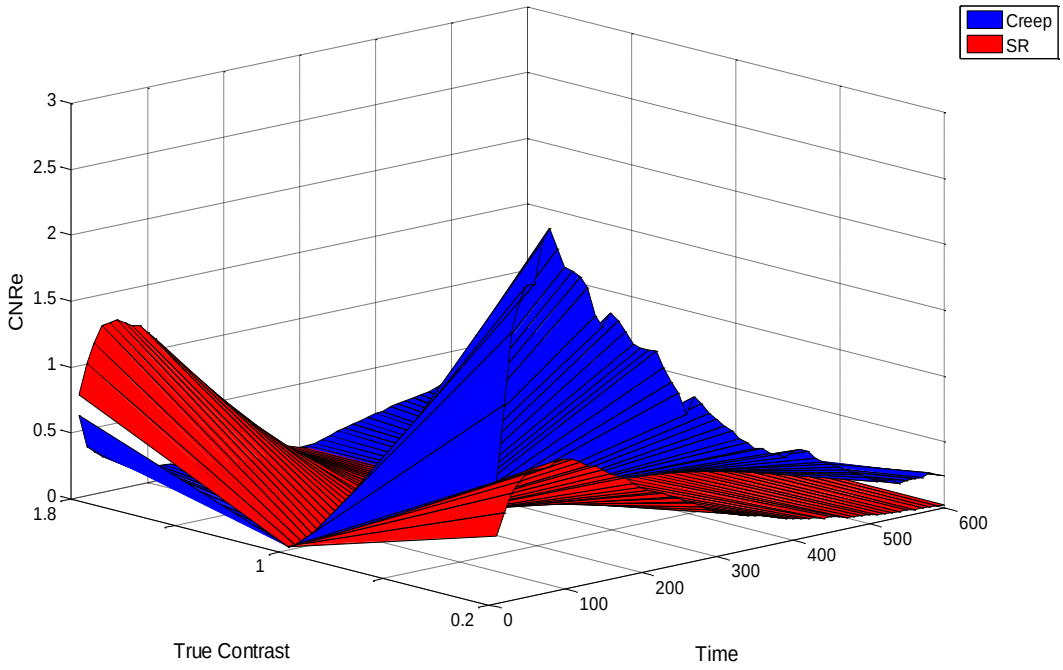


Fig 38. CNRe as a function of time and true underlying Poisson's ratio contrast for SR(red) and creep(blue)

*Statistical analysis for comparison between SR and creep*

Figures 39-40 show statistical comparison between SR and creep for Poisson's ratio contrast and Figure 41 shows the accuracy plot for this comparison.

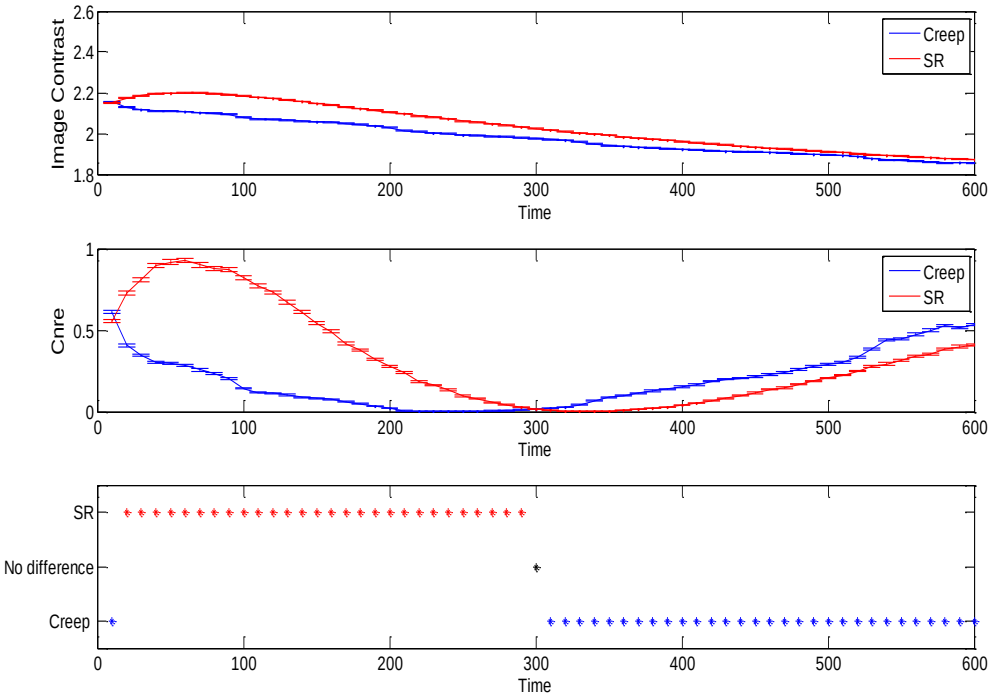


Figure 39. Statistical comparison of CNRe for 1.8 times Poisson's ratio contrast between inclusion and background .From top to bottom : Image contrast as a function of time for SR (red) and creep(blue) (error bars represent 95% confidence intervals) , CNRe as a function of time for SR (red) and creep(blue) (error bars represent 95% confidence intervals) and statistical comparison of the two compression techniques .

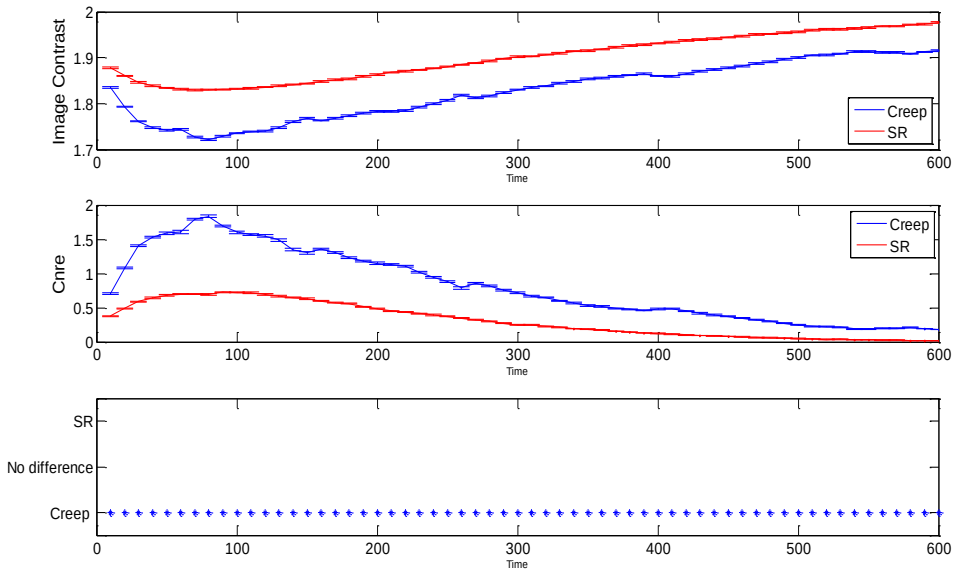


Figure 40. Statistical comparison of CNRe for 0.2 times Poisson's contrast between inclusion and background .From top to bottom : Image contrast as a function of time for SR (red) and creep(blue) (error bars represent 95% confidence intervals), CNRe as a function of time for SR (red) and creep(blue) (error bars represent 95% confidence intervals)and statistical comparison of the two compression techniques .

*Accuracy analysis for Poisson's ratio contrast*

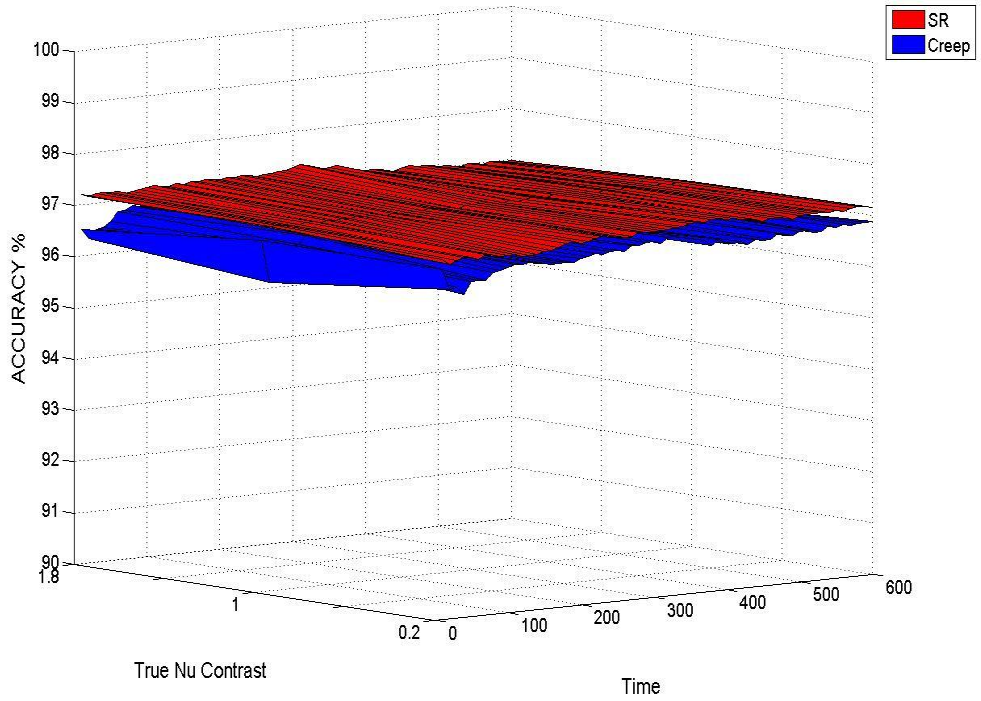


Fig 41 . Accuracy of axial strain poroelastograms for Poisson's ratio contrast.

*EPR poroelastograms*

Figures 42-43 show EPR poroelastograms for a undrained Poisson's ratio contrast of 1.8 and 0.2 respectively. Figure 44 shows the CNRe analysis plot , Figure 45 shows the accuracy plot and Figure 46 shows the CTE plot for these cases.

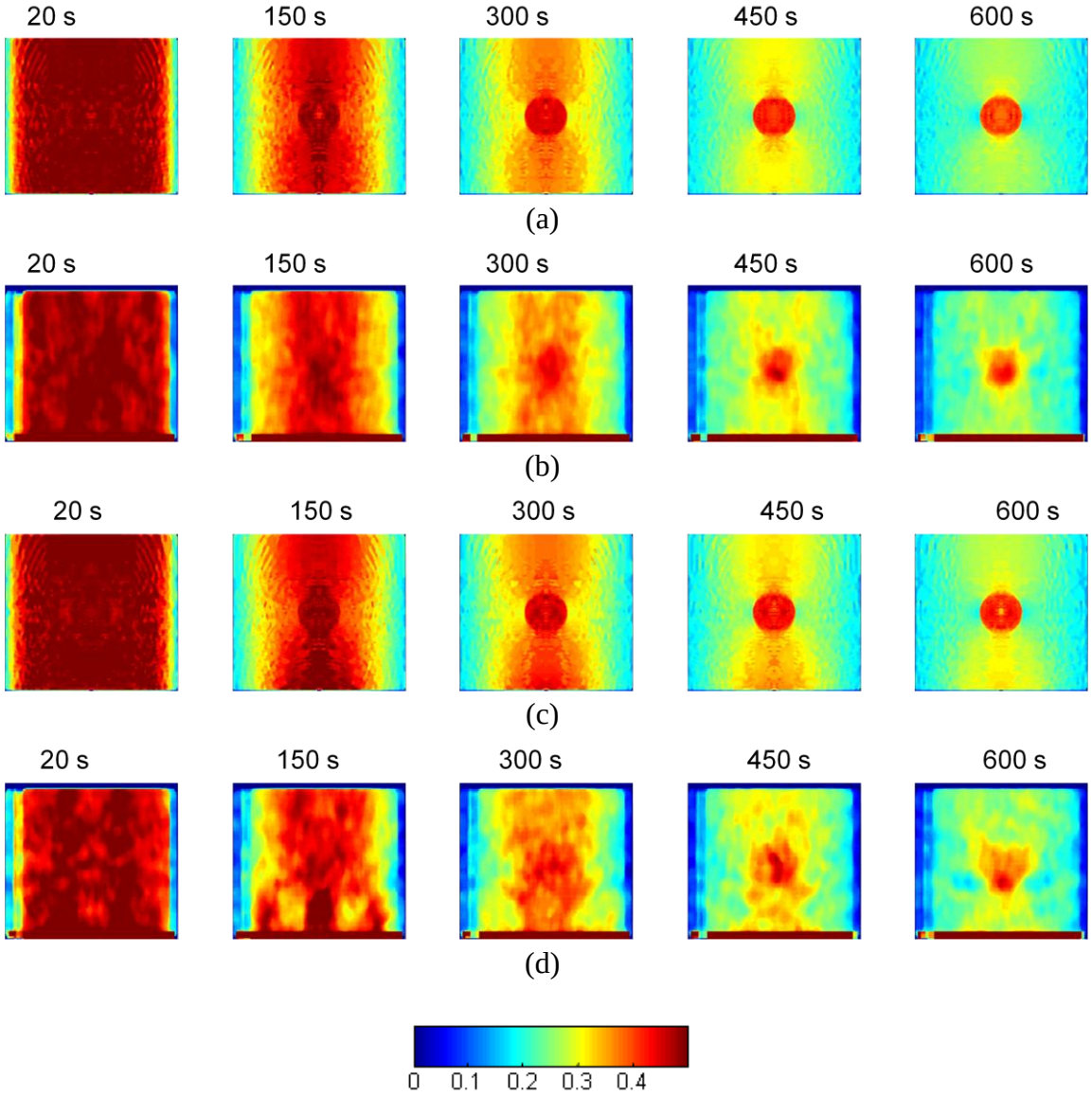


Figure 42. Time-sequenced EPR images for 1.8 times Poisson's ratio contrast between inclusion and background. (a) Ideal EPR maps obtained simulating SR loading conditions (b) EPR poroelastogram obtained simulating SR loading conditions (c) Ideal EPR maps obtained simulating creep loading conditions (d) EPR poroelastogram obtained simulating creep loading conditions. In each case, images are displayed for time values equal to 20s, 150s ,300s and 600s respectively.

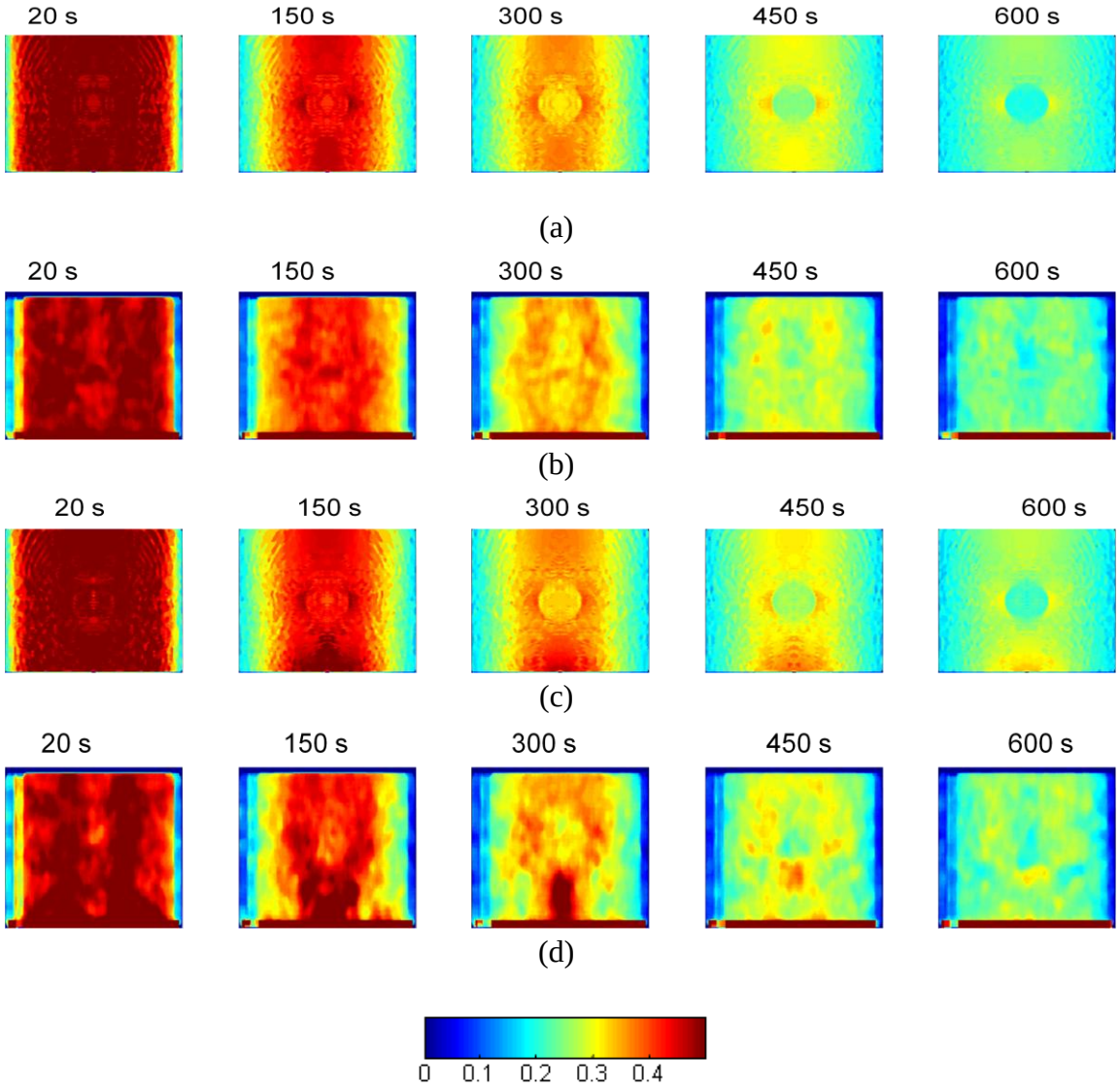


Figure 43. Time-sequenced EPR images for 0.2 times Poisson's ratio contrast between inclusion and background. (a) Ideal EPR maps obtained simulating SR loading conditions (b) EPR poroelastogram obtained simulating SR loading conditions (c) Ideal EPR maps obtained simulating creep loading conditions (d) EPR poroelastogram obtained simulating creep loading conditions. In each case, images are displayed for time values equal to 20s, 150s ,300s and 600s respectively.

*Poisson's ratio contrast EPR CNRe (PCNRe) analysis*

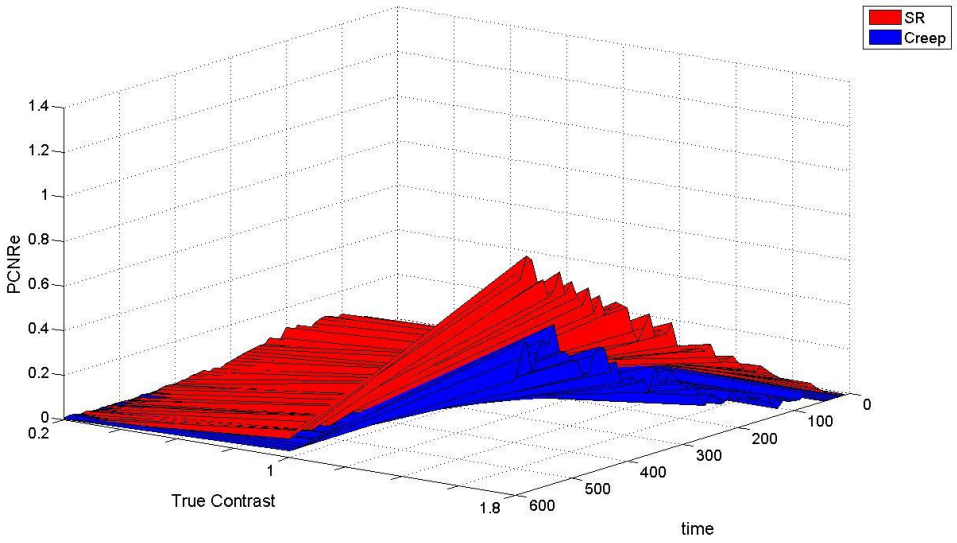


Fig 44. PCNRe plot for Poisson's ratio contrast showing PCNRe vs. time vs. true contrast for SR(red) and creep(blue).

*Poisson's Ratio contrast EPR accuracy analysis*

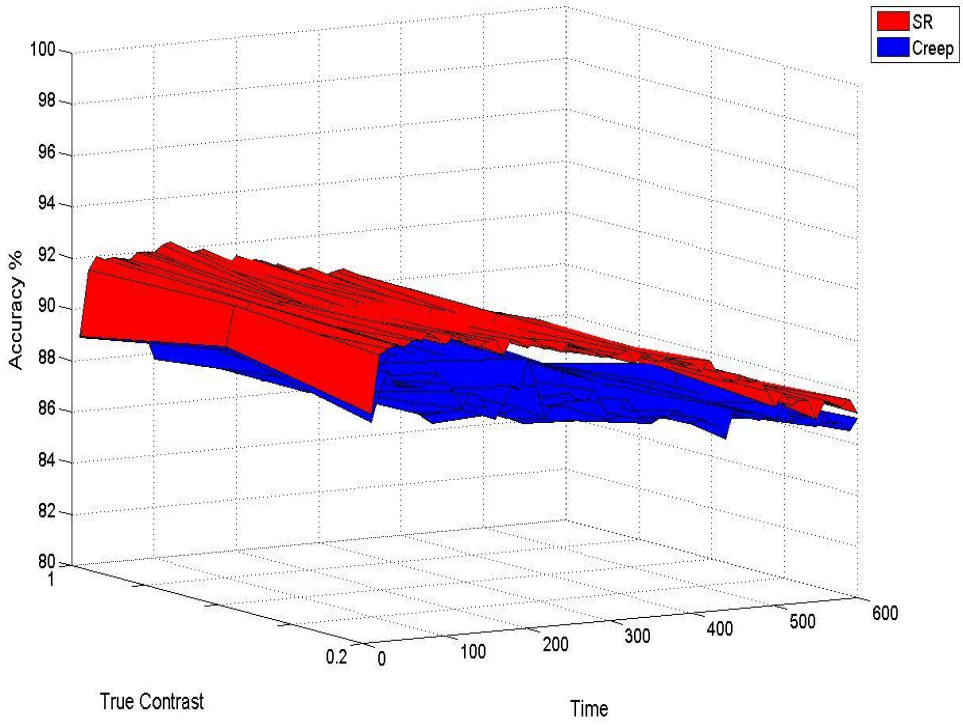


Fig 45.Accuracy of EPR poroelastogram for Poisson's ratio contrast showing accuracy vs. time vs. true contrast for SR(red) and creep(blue).

*Poisson's Ratio contrast EPR CTE analysis*

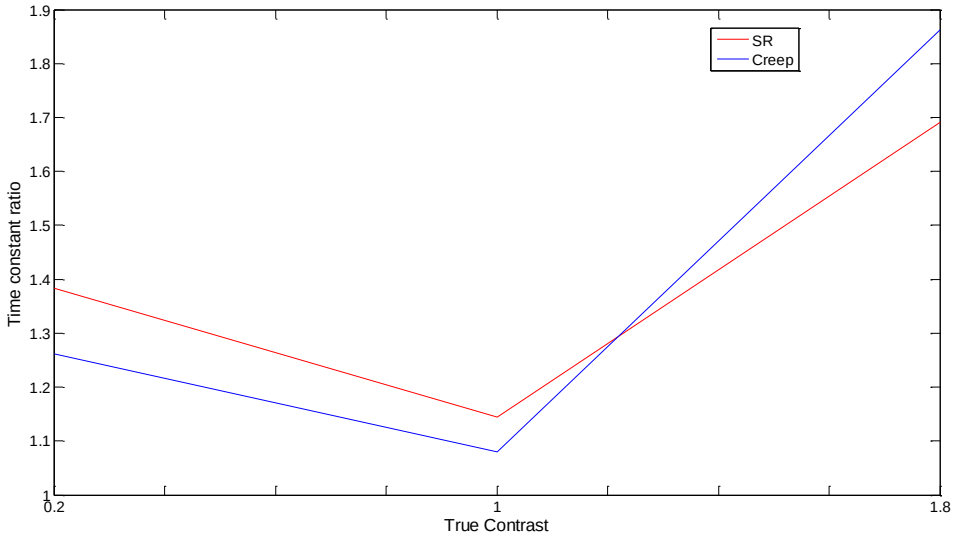


Fig 46. EPR CTE for Poisson's ratio contrast. Figure shows ratio of time constants on Y axis and the corresponding true contrast on X axis for SR(red) and creep(blue).

*Discussion of presented results*

Higher Poisson's ratio value implies lower compressibility of the solid matrix and vice versa. In the case where the inclusion solid matrix is less compressible, the axial strain is lower while the EPR poroelastogram follows the underlying Poisson's ratio contrast of the material. However, in the case where the solid matrix of the background is less compressible than the solid matrix of the inclusion, the material behaves as a homogeneous material. This is because the fluid movement from the inclusion is constrained by the background. Hence, although there exists an underlying

contrast of Poisson's ratio, the effective compressibility is governed by the background material.

CNRe values shown in Figure 38 are in general low in axial strain poroelastograms showing that underlying Poisson's ratio contrast produces a low contrast in corresponding axial strain elastograms. In the case of axial strain poroelastogram, the difference in CNRe for SR and creep is somewhat small. However for the PCNRe, SR leads to much higher PCNRe values than creep as shown in Figure 44. Accuracy for both axial strain and EPR poroelastograms is high as shown by Figures 41 and 45.

The CTE graph in Figure 46 shows that low compressible inclusion in a high compressible background can be more efficiently depicted in EPR poroelastogram than the reverse case. This may be due to reasons similar to the permeability contrast case as higher compressibility may imply a higher propensity to fluid flow.

# CHAPTER V

# CONCLUSION AND FUTURE WORK

In this chapter, I summarize the major results of this work and highlight areas that may need further investigation in the future.

## 1. Conclusion

The simulation study performs in this study confirms the original hypothesis that external and internal boundary conditions have a significant impact on the performance of poroelastography. External boundary conditions such as SR and creep loading lead to different performance parameters both for axial strain and EPR poroelastograms. For axial strain poroelastograms, in general creep has a statistically better performance than SR for most cases. For EPR poroelastograms, the opposite is true. However, the image quality analysis shows that differences between SR and creep, although statistically significant, are somewhat small and may be weighed with practical ease of use like availability of physical resources etc. while selecting a preferred method of compression.

The presence of an underlying poroelastic contrast between background and inclusion can have a major impact to both axial strain and EPR poroelastograms. In fact, all three poroelastic parameters considered in this study - permeability, Young's modulus and Poisson's ratio- individually, can affect poroelastographic images. This observation could have important implications for the development of tissue elasticity reconstruction methods as well as for the interpretation of images resulting from the

application of such methods. In addition, the effect of an underlying poroelastic contrast may or may not be significant depending on the relative properties of the inclusion with respect to the background. For example, the presence of a background less permeable than the inclusion restricts fluid flow from the inclusion and, effectively, the overall material appears as a homogenous material both in the axial strain and in the EPR poroelastograms. Similar considerations have been carried out also for the case of an underlying Young's modulus contrast or Poisson's ratio contrast.

## 2. Future Work

*3D poroelastography*

The 2-D model studied in this work may be extended to analyze fluid flow in all three dimensions. The 3-D model may give a more realistic view of what we may expect *in-vivo.*

*Modeling of complex mechanical geometries*

In this study, I analyzed a simplistic cubical geometry with a cylindrical inclusion and frictionless boundary conditions. In the future, different geometries that may better resemble certain complex tissues should be investigated as well. As a step toward this goal, I obtained preliminary results for a case of a medium composed by two layers of poroelastic materials with different mechanical properties. Fig 47 shows the axial strain and EPR ratio poroelastogram for this case. This geometry could resemble a subcutaneous/muscle tissue layer. Since an important application of poroelastography is to distinguish between lymphedematous and non-lymphedematous tissues *in vivo*

(Righetti et. al 2007b), a thorough study using this geometrical configuration could be of great value.

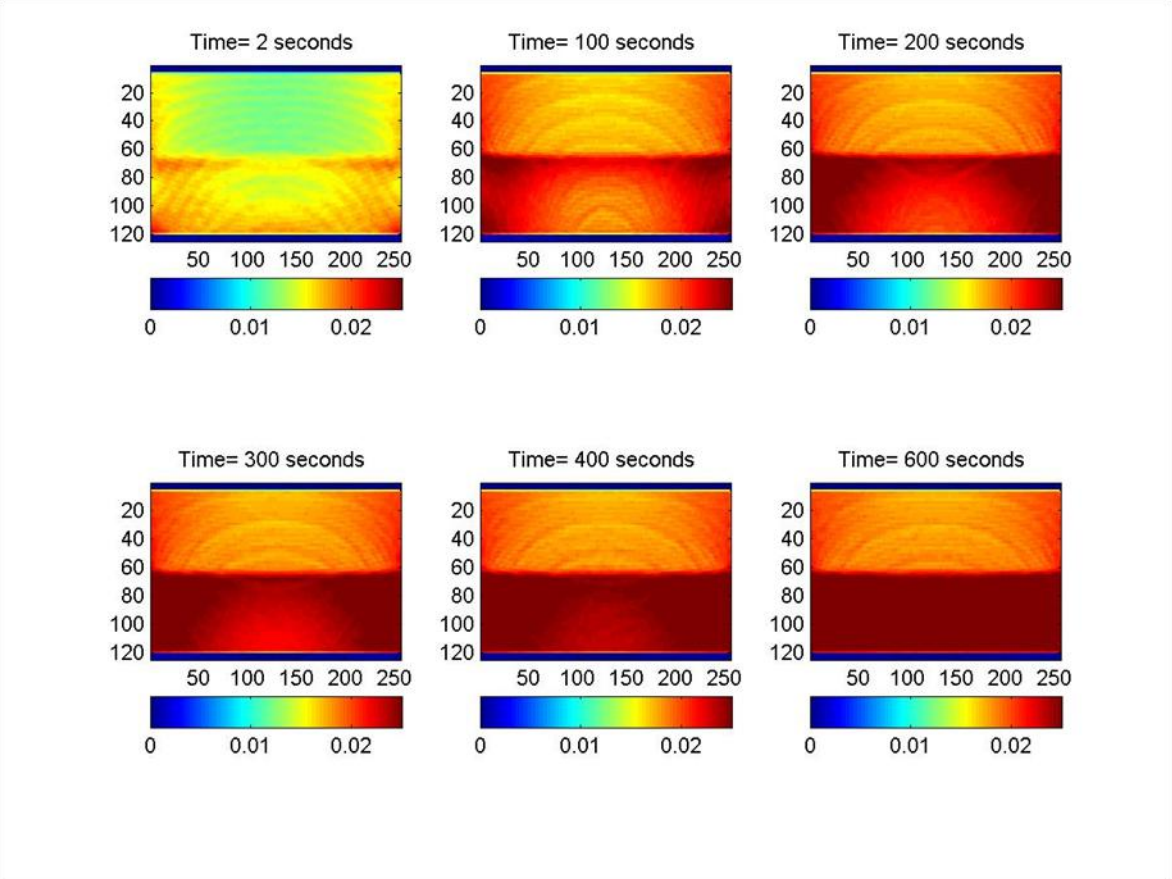


Fig 47. Axial Strain poroelastogram of a poroelastic bi-layer material.

In simulation studies involving inclusions (such as the one presented in this thesis), boundary conditions can be varied to simulate more realistic in vivo situation. For example, instead of a frictionless base a fixed base or a confinement from one or

more sides can also be modeled. I initiated the investigation of with a model with fixed base boundary conditions. Fig 48 shows the corresponding axial stain poroelastogram.

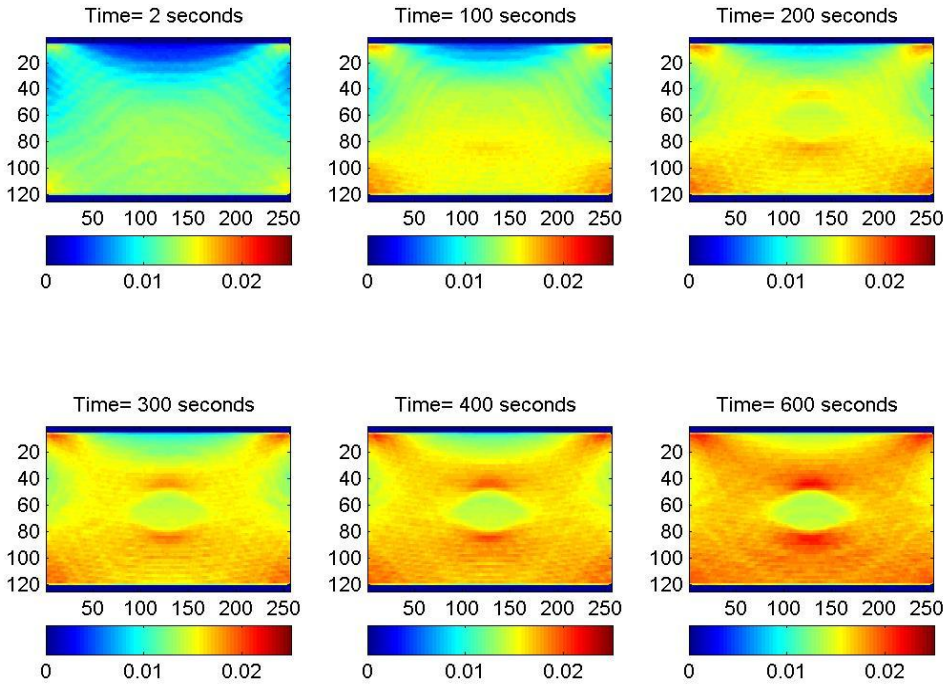


Fig 48. Axial Strain poroelastogram of a poroelastic material with -40 db permeability contrast between inclusion and background with fixed base boundary condition (instead of slippery).

*Experimental validation*

This work presents a simulation study to analyze the effects of internal and external boundary conditions on poroelastography. It is advisable in the future to

corroborate the results using controlled experimental data. It is possible that performing experiments may lead to a modification of the proposed simulation models to better match the experimental conditions. Although a modification of the proposed simulation model is likely to affect the image quality results, it is expected that the major conclusions supported by this work would still be valid.

*Feasibility of poroelastography to image interstitial hypertension in solid tumors*

Interstitial hypertension has been shown to be highly correlated with presence of soft tissue tumors and is one of the most impeding factors in drug delivery (Less et al. 1992). Many tumors can be modeled as poroelastic solids (Netti et al. 1995). Tumor hypertension maybe due to tissue fibrosis or a collapse of the interstitial matrix. Both of them significantly reduce the permeability of the tissue. Tumors have been shown to have significantly lower permeability coefficients with respect to normal tissue ,which is a major reason for causing elevated Interstitial Fluid Pressure (IFP) (Milosevic et al. 2008, Boucher et al. 1990).Poisson's ratio itself has been shown to be related to the pore pressure in non-biological materials (Carcione and Cavallini 2002). In this simulation study, I observed a high correlation between EPR poroelastograms and interstitial fluid pressure maps (provided by the mechanical model) suggesting that it may be feasible to use poroelastography for mapping interstitial hypertension. As an example supporting this observation, Fig 49 shows a pore pressure maps and EPR maps corresponding to a model in which the permeability of the inclusion is lower compared to the background. Note that the inclusion can be clearly seen with time in both sets of images. Note also that the EPR of the inclusion does not change from the undrained value, suggesting

infinitesimal slow fluid flow out of the inclusion, which is a direct consequence of the elevated IFP.

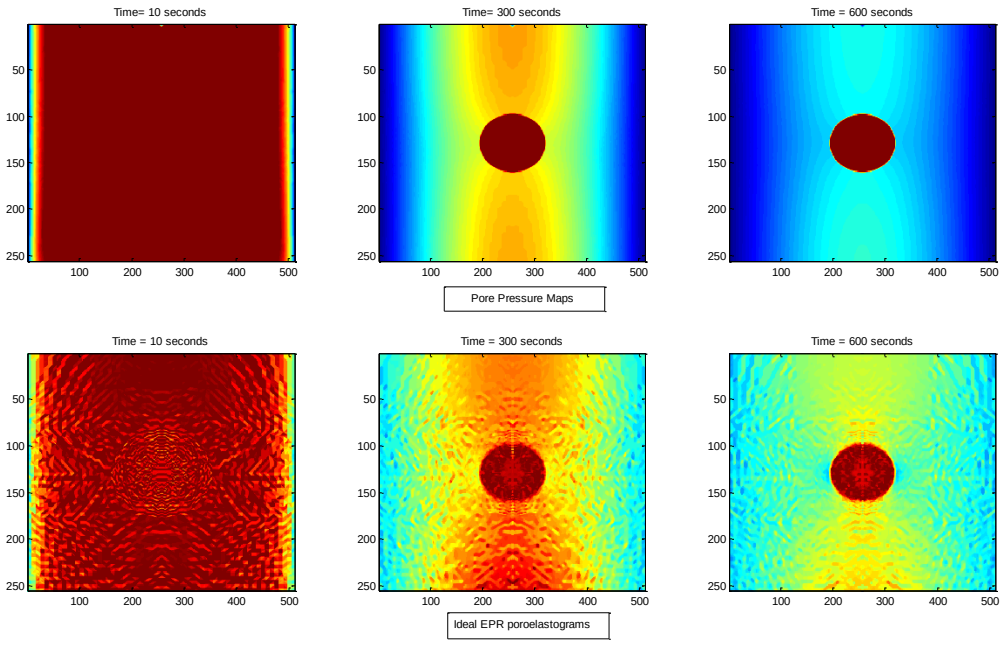


Fig 49. Pore pressure distribution (top row) and the corresponding EPR maps.

Thus in the future, poroelastographic techniques may be extended to image additional parameters , which might be very prove clinically useful for the diagnosis and staging of various pathologies.

# REFERENCES

Armstrong CG, Lai WM, Mow VC. An analysis of the unconfined compression of particular cartilage. J Biomech Eng., 1984; 106: 165-173.

Armstrong CG, Mow VC. Variations in the intrinsic mechanical properties of human particular cartilage with age, degeneration, and water-content. J Bone Joint Surgery, 1982; 64(1): 88-94.

Bendat JS and. Piersol AG, Random data: Analysis and measurement procedures, New York: John Wiley and Sons; 2000.

Berry GP, Bamber JC, Armstrong CG, Miller NR, Barbone PE. Towards an acoustic model-based poroelastic imaging method: I. Theoretical foundation. Ultras. Med. Biol., 2006a; 32(4): 547-567.

Berry GP, Bamber JC, Miller NR, Barbone PE, Bush NL, Armstrong CG. Towards an acoustic model-based poroelastic imaging method: II. Experimental investigation. Ultras. Med. Biol., 2006b; 32(12): 1869-1885.

Biot MA. General theory of three-dimensional consolidation, J. Appl. Phys 1941; 12: 155-164.

Biot MA. Le problème de la consolidation des matières argileuses sous une charge, Ann. Soc. Sci. Bruxelles 1935; B55: 110-113.

Boucher Y, Baxter LT and Jain RK. Interstitial pressure gradients in tissue isolated and subcutaneous tumors: implications for therapy. Cancer Res., 1990; 50: 4478-4484.

Bowen RM. Compressible porous media models by use of the theory of mixtures, Int. J. Engng. Sci., 1982; 20: 697-735.

Carcione JM and Cavallini F. Poisson's ratio at high pore pressure. Geophysical Prospecting, 2002; 50: 97–106. doi: 10.1046/j.1365-2478.2002.00299.

Darcy H. Les fontaines publiques de la ville de Djion, Paris: Dalmont;1856.

Detournay E and Cheng, AHD. Fundamentals of poroelasticity: In C. Fairhurst(ed.) Comprehensive rock engineering: Principles, practice and projects, Vol. II, Analysis and Design Method: Pergamon Press; 1993;p 113-171.

Fatt I. Dynamics of water transport in the corneal stroma. Exp. Eye. Res., 1968; 7: 402-412.

Folkman J. The role of angiogenesis in tumor growth. Semin. Cancer Biol. 1992; 3: 65-71.

Fortin M, Buschmann MD, Bertrand MJ, Foster FS, Ophir J. Dynamic measurement of internal solid displacement in articular cartilage using ultrasound backscatter. J. Biomech., 2003; 36(3): 443-447.

Kallel F, Bertrand M and Ophir J. Fundamental limitations on the contrast transfer efficiency in elastography – an analytic study. Ultrasound in Medicine and Biology , 1996 ;22 :463-470 .

Khosravani H, Chugh B, Milosevic M and Norwhich K. Time response of interstitial fluid pressure measurements in cervix cancer, Microvasc.2004; 68: 63–70.

Konofagou EE, Harrigan TP, Ophir J, Krouskop TA. Poroelastography: imaging the poroelastic properties of tissues. Ultras Med Biol., 2001; 27: 1387-1397.

Less RJ, Posner MC, Boucher Y, Borochovitz D, Wolmark N and Jain RK.Interstitial hypertension in human breast and colorectal tumors. Cancer Res. 1992; 52: 6371 -6374.

Liederman R and Barbone P. Coupling between elastic strain and interstitial fluid flow: ramifications for poroelastic imaging, Physics in Medicine and Biology , 2006; 51 : 6291–6313.

Milosevic M, Lunt S and Hill R. Interstitial permeability and elasticity in human cervix cancer. Microvascular research 2008;75: 381-390.

Mow VC, Kuei SC, Lai WM. and Armstrong CG. Biphasic creep and stress relaxation of articular cartilage in compression: theory and experiments, J. Biomech. Eng., 1980;102 :73-84.

Mridha M and Ödman S. Noninvasive method for assessment of subcutaneous edema. Med. and Biol. Eng. and Comp., 1986 ;24: 393-398.

Nair SP. Performance analysis of a new ultrasound axial strain time constant estimation, A Master's Thesis, Texas A&M University, College Station, TX, 2010.

Netti PA, Baxter LT, Boucher Y, Skalak R and Jain RK Time-dependent behavior of interstitial fluid pressure in solid tumors: implications for drug delivery Cancer Res. 1995; 55:5451–5458.

Ophir J, Alam K, Garra B, Kallel F, Konofagou EE, Krouskop TA and Varghese T. Elastography: ultrasonic estimation and imaging of the elastic properties of

tissues. Proceedings of the Institution of Mechanical Engineers, Part H Journal of Engineering in Medicine. 1999; 1-31.

Ophir J, Céspedes EI, Ponnekanti H, Yazdi Y and Li X. Elastography: a quantitative method for imaging the elasticity of biological tissues. Ultrasonic Imaging. 1991; 13:111-134.

Park J. Liposome based drug delivery in breast cancer treatment. Breast cancer res . 2002 ;4: 95-99 .

Ponnekanti H, Ophir J, Huang Y and Céspedes I. Fundamental mechanical limitations on the visualization of elasticity contrast in elastography. *Ultrasound Med Biol* 1995; 21:533–543.

Qiu Y, Sridhar M, Tsou JK, Lindfors K and Insana M. Ultrasonic viscoelasticity imaging of nonpalpable breast tumors: preliminary results. Acad Radiol 2008; 15:1526-1533.

Rice JR and Cleary MP. Some basic stress-diffusion solutions for fluid saturated elastic porous media with compressible constituents, Rev. Geophys. Space Phys. 1976; 14: 241.

Righetti R, Ophir J, Srinivasan S  Krouskop TA. The feasibility of using elastography for imaging the Poisson's ratio in porous media.  Ultras Med Biol., 2004; 30: 215-228

Righetti R, Ophir J and Krouskop TA. A method for generating permeability elastograms and Poisson's ratio time-constant elastograms. Ultras. Med. Biol., 2005 ;31(6): 803-816.

Righetti R, Righetti M, Ophir J and Krouskop TA. The feasibility of estimating and imaging the mechanical behavior of poroelastic materials using axial strain elastography. Phys. Med. Biol., 2007a; 52(11): 3241-3259.

Righetti R, Srinivasan S, Thitai Kumar A, Ophir J and Krouskop TA. Assessing image quality in effective Poisson's ratio elastography and poroelastography – Part I. Physics Med. Biol., 2007b; 52: 1303-1320.

Srinath S. Comparison of the Performance of Different Time Delay Estimation Techniques for Ultrasound Elastography, A Master's Thesis, Texas A&M University, College Station, TX, 2010.

Srinivasan S, Ophir J and Alam SK. Elastographic imaging using staggered strain estimates, Ultrasound in Med. & Biol., 2002; 24 :224:245.

Srinivasan S, Righetti R, and Ophir J. Tradeoffs between signal to noise ratio and axial resolution in ultrasound elastography, Ultrasound in Med. & Biol., 2003; 296: 847–866.

Terzaghi, K. Die berechnung der durchlassigkeitsziffer des tones aus dem verlauf der hydrodynamischen spannungserscheinungen, Sitz. Akad. Wissen., Wien Math. Naturwiss. 1923 ;132: 105-124.

Van Houten EEW, Doyley MM, Kennedy FE, Weaver JB, Paulsen KD. Initial in vivo experience with steady-state subzone-based MR elastography of the human breast. J. Magn. Reson. Imag., 2003;17: 72-85.

Varghese T, Ohir J, Konofagou EE, Kallel F and Righetti R. Tradeoffs in elastographic imaging. Ultrasonic Imaging. 2001; 23: 216-248.

Varghese T and Ophir J. Enhancement of echo-signal correlation in elastography using temporal stretching, IEEE Transactions on Ultrasonics, Ferroelectrics, and Frequency Control, 1997; 44 :173-180.

Wang HF. Theory of linear poroelasticity. Princeton NJ. Princeton University Press, 2000.

Yang X, Deka S and Righetti R. Elastography on GPGPU for real-time applications. Proceedings of the 8th International Conference on the ultrasonic measurement and imaging of tissue, Vlissingen, Zeeland, The Netherlands, Sept. 14-17 2009. P 47.

# APPENDIX A

*Axial Strain Image (Elastogram)*

It is a single image showing axial strain distribution which in the case of poroelastography represents the local "effective stiffness" of the phantom.

*Axial Strain Poroelastogram*

An axial strain poroelastogram is a series of time-sequenced axial strain elastograms obtained at sampled time intervals following after compression. In this study the window of observation is 600 seconds and we generate an elastogram every 10 seconds.

*Effective Poisson's Ratio (EPR) Elastogram*

An EPR elastogram is an image obtained by dividing pixels in the lateral strain elastogram by corresponding pixels in the axial strain elastogram. In a poroelastic material, the EPR elastogram represents the estimated EPR distribution of the material under compression and is a map of the local effective compressibility.

*Poroelastogram*

A poroelastogram is a series of time-sequenced EPR elastograms obtained from the poroelastic material at sampled time intervals after compression. They convey information about the local time-dependent changes of the effective compressibility and fluid movement within the imaged material due to the application of the load. As in the case of axial strain poroelastogram, EPR poroelastogram is generated every 10 seconds up to 600 seconds.

# VITA


| | |
|---|---|
| Name: | Anuj Chaudhry |
| Address: | Department of Electrical and Computer Engineering<br>2365-H WERC<br>3128 TAMU<br>College Station, Texas, 77843-3128 |
| Email address: | Anuj127@.tamu.edu |
| Education: | B.E., Biomedical Engineering, Mumbai University, India<br>M.S., Electrical Engineering, Texas A&M University |